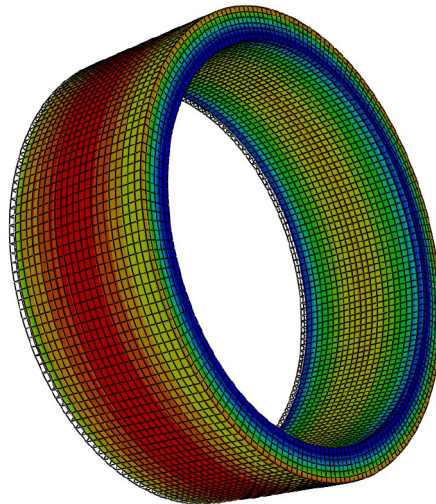




CHALMERS
UNIVERSITY OF TECHNOLOGY



A method for characterization of elastic in-plane material properties of continuous fiber reinforced polymer tubes

Master's thesis in Applied Mechanics

JOHN BORENIUS
TOBIAS BREDEBERG

MASTER'S THESIS IN APPLIED MECHANICS

**A method for characterization of elastic in-plane
material properties of continuous fiber reinforced
polymer tubes**

JOHN BORENIUS
TOBIAS BREDEBERG



CHALMERS
UNIVERSITY OF TECHNOLOGY

Department of Industrial and Materials Science
Division of Material and Computational Mechanics
CHALMERS UNIVERSITY OF TECHNOLOGY
Gothenburg, Sweden 2020

A method for characterization of elastic in-plane material properties of continuous fiber reinforced polymer tubes

JOHN BORENIUS

TOBIAS BREDENBERG

© JOHN BORENIUS, TOBIAS BREDENBERG, 2020.

Supervisor: Martin Fagerström, Department of Industrial and Materials Science

Examiner: Brina Blinzler, Department of Industrial and Materials Science

Department of Industrial and Materials Science
Division of Material and Computational Mechanics
Chalmers University of Technology
SE-412 96 Gothenburg
Telephone +46 31 772 1000

Cover: Visualization of the stress distribution of a composite ring in compression (Abaqus CAE).

Typeset in L^AT_EX

Printed by Chalmers digitaltryck

Gothenburg, Sweden 2020

A method for characterization of elastic in-plane material properties of continuous fiber reinforced polymer tubes

JOHN BORENIUS

TOBIAS BREDENBERG

Department of Industrial and Materials Science

Chalmers University of Technology

Abstract

As fiber reinforced polymers are becoming commonplace in more and more industries every year, the need for accurate engineering tools connected to these materials arises. In several industries tubular composites are a staple, however the manufacturing methods used for tubular laminated composites do not transfer well into making test coupons for traditional material testing. This creates the need for a method where material properties can be derived from testing of tubular specimen. This thesis therefore aims to create a method for characterizing the elastic in-plane material properties of a tubular fiber reinforced composite. The method uses physical tests of two specific lay ups in order to isolate and derive the in-plane material properties one by one. The results of this thesis shows that the material properties derived from the test data is within close proximity of other material systems using the same fibers, which suggests that a promising first step has been taken. However, there is a need for validation in order to finalize the accuracy of the model. Furthermore a number of practical suggestions are made to reduce error sources for future testing.

Keywords: material characterization, composite, tube, pipe, elastic, carbon fiber, CFRP, finite element

Acknowledgements

This master thesis was done at the Department of Industrial and Materials Science, Chalmers University of Technology.

We would like to give a special thanks to our examiner Brina Blinzler and supervisor Martin Fagerström for your support and help along the way. We would also like to thank *Easton Diamond Sports Ltd.* for providing the test samples, Carolyn Oddy for some helpful instructions and Carlos Lindau at *LISAB* for providing help and guidance with measuring equipment.

John Borenus and Tobias Bredenberg, Gothenburg, June 2020

Contents

List of Figures	xi
List of Tables	xv
1 Introduction	1
2 Theory	3
2.1 Composites	3
2.1.1 Orthotropic properties	4
2.1.2 Element types in Abaqus	5
2.1.2.1 Eight-noded solid element C3D8	5
2.1.2.2 Eight-noded solid element - reduced integration C3D8R	6
2.1.2.3 Twenty-noded solid element C3D20	6
2.1.2.4 Twenty-noded solid element - reduced integration C3D20R	7
3 Methods	9
3.1 Choice of lay-ups and material systems	9
3.2 Choice of physical tests	9
3.2.1 FE model	10
3.2.2 Mesh dependency	14
3.2.3 Analysis of axial compression test	16
3.2.4 Analysis of split hoop test	21
3.2.5 In-plane shear modulus	25
3.3 Modeling of the test rigs	27
3.4 Building of rig	29
3.5 Preparing samples	30
3.6 Physical testing	31
3.7 Data handling	34
3.8 Material characterization	34
4 Results and discussion	37
4.1 Raw physical test data	37
4.2 Analyzed physical test data	41
4.3 Final results using characterized parameters	46
4.4 Sources of error	50
5 Conclusion and proposed validation	51
5.1 Investigation of potential validation	51
5.2 Conclusion	54
5.3 Future considerations	55

List of Figures

2.1	Stacking direction for a $[90/\pm 80/90]$ composite lay-up in Abaqus. The principal direction 1 is referred to as the z-axis, 2 is φ -axis and 3 is r -axis.	3
2.2	Example for a three ply composite with three integration points per layer [1].	5
2.3	C3D8: A general purpose fully integrated eight-node brick element [2].	6
2.4	C3D8R: A general purpose eight-node brick element with reduced integration [3].	6
2.5	C3D20: A general purpose fully integrated twenty-node brick element [4].	7
2.6	C3D20R: A general purpose twenty-node brick element with reduced integration [5].	7
3.1	Initial comparison of different FE models with symmetry boundary conditions and area of strain measurement marked in red.	12
3.2	Simulated average circumferential strain in the split hoop test for different FE models.	13
3.3	Simulated average axial strain in the split hoop test for different FE models.	14
3.4	Figure showing mesh dependency study for split hoop test based on global element size and circumferential strain.	15
3.5	Figure showing mesh dependency study for axial compression test based on global element size and axial strain.	16
3.6	Figure showing show axial and circumferential strains vary across the hoops, showing edge effects.	17
3.7	Sensitivity of average maximum axial strain due to different ν_{LT} in axial compression.	18
3.8	Sensitivity on the maximum averaged axial strain with respect to different E_L in axial compression.	19
3.9	Force response for a set displacement with changed ply orientations on tube $T1$. The angle is measured from the axial direction on the tube.	20
3.10	Sensitivity on circumferential strain with respect to different E_T in split hoop test.	21
3.11	Sensitivity on circumferential strain with respect to different ν_{LT} in split hoop test.	22
3.12	Sensitivity on circumferential strain with respect to different friction coefficient μ in split hoop test.	23
3.13	Sensitivity on the averaged maximum circumferential strain with respect to different ν_{LT} in axial compression.	24
3.14	Sensitivity on the averaged maximum axial strain with respect to different ν_{LT} in the split hoop test.	25
3.15	Averaged maximum circumferential strain when varying E_L on tube $T3$ in the split hoop test.	26

3.16	Averaged maximum circumferential stress when varying ν_{LT} on tube $T3$ in the split hoop test.	26
3.17	Averaged maximum circumferential stress when varying G_{LT} on tube $T3$	27
3.18	Drawing of the split hoop rig used for testing.	28
3.19	Figure showing the stress distribution in the rig, with hot spots at the pin-plate interface	28
3.20	Drawings of the compression test rig used for testing	29
3.21	Pictures of hoop surfaces during surface preparation.	30
3.22	Picture showing a strain gauge mounted on a hoop.	31
3.23	Picture showing the split hoop setup and extensometer placing.	32
3.24	Picture showing axial compression test.	33
3.25	Picture showing the angular deformation of the pins in the split hoop fixture.	33
4.1	Figure showing relation between applied force and measured axial strain for the five test specimens of $T1$ in axial compression.	37
4.2	Figure showing relation between applied force and measured circumferential strain for the five test specimens of $T1$ in axial compression.	38
4.3	Figure showing relation between applied force and measured circumferential strain for the five test specimens of $T1$ in the split hoop test.	39
4.4	Figure showing relation between applied force and measured axial strain for the five test specimens of $T1$ in the split hoop test.	40
4.5	Figure showing relation between applied force and measured circumferential strain for the five test specimens of $T3$ in the split hoop test.	40
4.6	Figure showing the most linear force-axial strain relation in the axial compression test on tube $T1$, which occurs in the load region between 25 and 35 kN (indicated by the black dotted lines). The black circles represent an linear response using the mean linear slope in that region.	41
4.7	Figure showing the most linear force-circumferential strain relation in the axial compression test on tube $T1$, which occurs in the load region between 25 and 35 kN (indicated by the black dotted lines). The black circles represent an linear response using the mean linear slope in that region.	42
4.8	Figure showing the most linear force-circumferential strain relation in the split hoop test on tube $T1$, which occurs in the load region between 35 and 45 kN (indicated by the black dotted lines). The black circles represent an linear response using the mean linear slope in that region.	43
4.9	Figure showing the most linear force-axial strain relation in the split hoop test on tube $T1$, which occurs in the load region between 15 and 25 kN (indicated by the black dotted lines). The black circles represent an linear response using the mean linear slope in that region.	44

4.10	Figure showing the most linear force-circumferential strain relation in the split hoop test on tube $T3$, which occurs in the load region between 0 and 10 kN (indicated by the black dotted lines). The black circles represent an linear response using the mean linear slope in that region.	45
4.11	Figure showing axial strain on tube $T1$ from both physical test results and a simulation using calibrated material parameters in axial compression.	46
4.12	Figure showing circumferential strain on tube $T1$ from both physical test results and a simulation using calibrated material parameters in axial compression.	47
4.13	Figure showing circumferential strain on tube $T1$ from both physical test results and a simulation using calibrated material parameters in the split hoop test.	48
4.14	Figure showing axial strain on tube $T1$ from both physical test results and a simulation using calibrated material parameters in the split hoop test.	49
4.15	Figure showing circumferential strain on tube $T3$ from both physical test results and a simulation using calibrated material parameters in the split hoop test.	49
5.1	Numerical response of the proposed bi-axial validation test showing the evolution of circumferential strain as a function of increasing load, and its sensitivity to the longitudinal stiffness E_L	52
5.2	Numerical response of the proposed bi-axial validation test showing the evolution of axial strain as a function of increasing load, and its sensitivity to the longitudinal stiffness E_L	52
5.3	Numerical response of the proposed bi-axial validation test showing the evolution of circumferential strain as a function of increasing load, and its sensitivity to the transverse stiffness E_T	53
5.4	Numerical response of the proposed bi-axial validation test showing the evolution of circumferential strain as a function of increasing load, and its sensitivity to the Poisson's ratio ν_{LT}	53
5.5	Numerical response of the proposed bi-axial validation test showing the evolution of shear strain as a function of increasing load, and its sensitivity to the shear modulus G_{LT}	54
5.6	Flowchart of the proposed workflow of the method created in this thesis	55

List of Tables

3.1	Layups for the provided carbon tubes.	9
3.2	Standard modulus carbon fiber data.	10
3.3	Epoxy matrix data.	10
3.4	Normalized lamina data for initial tests calculated with RoM.	10
3.5	Table showing element values and computational time from mesh sensitivity study	15
3.6	List of tolerances used in fminsearch.	34

Nomenclature

Abbreviations

FAW	Fiber area weight
FE	Finite element
GUI	Graphical user interface
RoM	Rule of mixtures

Description

Abaqus	Software for computer aided engineering
apparent stiffness	Stress over strain slope at a certain point of the material (not a real stiffness)
axial	Along the direction of the tubes
fmincon	General optimization function in MATLAB
fminsearch	Non-derivative optimization function in MATLAB
MATLAB	Programming language for scientific applications
Python	General programming language

Indicies

f	Fiber; referring to reinforcing fibers of composite
L	Longitudinal; along fiber direction
m	Matrix; referring to bonding matrix of composite
T	Transverse; perpendicular to fiber direction
LT	Along directions of transverse isotropy

Symbols

μ	Friction coefficient
ν	Poisson's ratio
E	Stiffness modulus
G	Shear modulus

1

Introduction

As material science constantly moves forward the use of fiber reinforced polymers becomes more commonplace each year. The use of fiber reinforced composites makes for an exceptional opportunity to engineer parts in a way which was never possible with regular isotropic materials. The rise of this new opportunity to engineer composite layups for specific parts creates the need for accurate material models, since without these models the benefit of being able to design part specific stiffness disappears as model predictions will be inaccurate.

A common place to use fiber reinforced polymers are tubular pipes and beams which are usually manufactured using methods such as bladder moulding, filament winding or pipe wrapping, which are not suitable for making flat test coupons for classical material testing. There are examples of these processes being used for flat parts [6], [7], however new equipment needs to be manufactured and it is not certain that the flat parts will have the exact same material composition as the tubular parts in production. Due to these circumstances a need for material testing with the use of tubular specimen has arisen. This thesis therefore aims to create a method for extracting the elastic in-plane material properties of tubular fiber reinforced polymer specimen.

The main objective to characterize material properties of company specific bladder moulded material systems and the tubular material necessary for this thesis was provided by *Easton Diamond Sports Ltd.* at the beginning of this project. Due to the current Covid-19 situation this collaboration was cut short and the aim of the thesis moved from a company specific material characterization to creating a method for general material characterization of tubular fiber reinforced polymers. The need for this type of simplified method is supported by the fact that most studies found are using multiple complex machines and testing methods such as pressurizing, as well as using other types of manufacturing methods and looking for other more specific properties such as breaking strength or impact resistance [7], [8], [9], [10], [11]. Furthermore none of the studies found presents a clear method for general material characterization.

2

Theory

This chapter describes the relevant theory about composite lay-ups and FE-model settings such as integration points and element types.

2.1 Composites

A composite laminate contains multiple layers of unidirectional fibers bonded together with a polymer matrix. Each layer is referred to as ply or lamina and these can be stacked in different orientations to obtain the desired properties for the composite. The stacked sheets are then referred to as a laminate with the desired properties from the stacking orientation that is also referred to as the lay-up.

In a cylindrical coordinate system, the lay-up sequence is considered positive in the radial direction (3) with a zero degree angle in the longitudinal z -axis (1) as in Figure 2.1. The out-of-plane axis of rotation of the plies will be in r -direction.

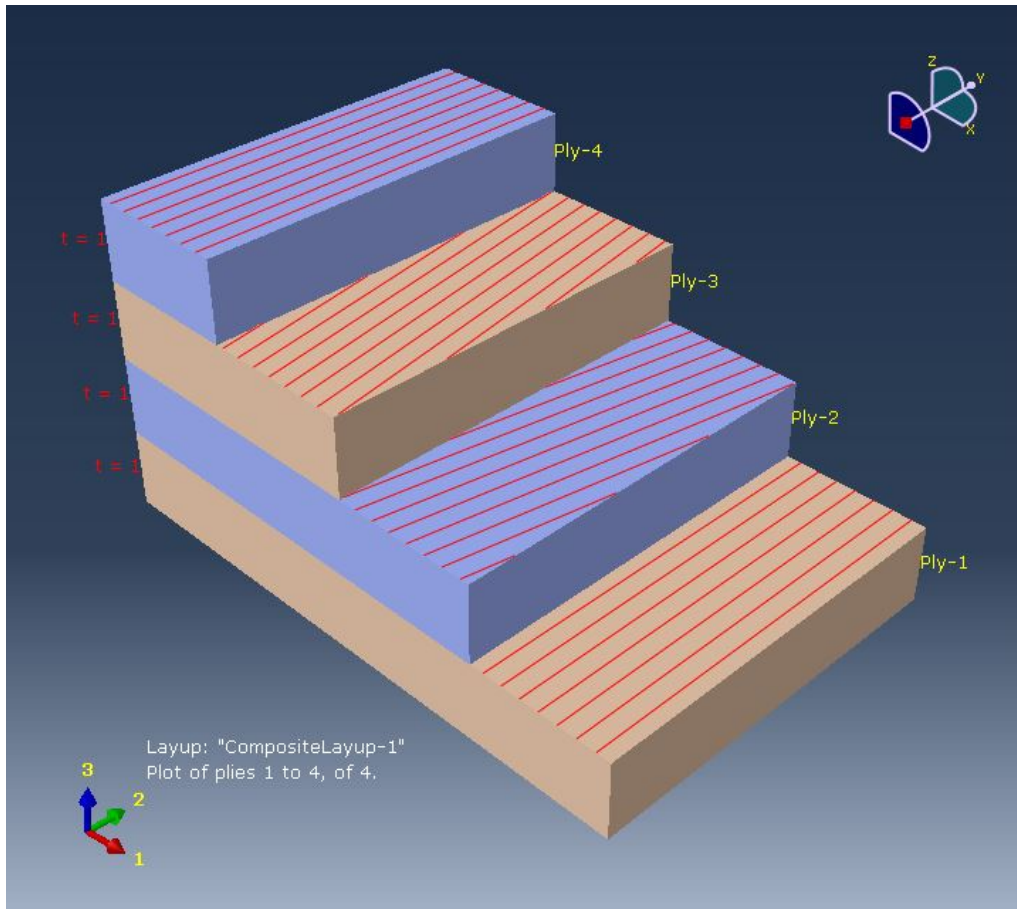


Figure 2.1: Stacking direction for a $[90/\pm 80/90]$ composite lay-up in Abaqus. The principal direction 1 is referred to as the z -axis, 2 is φ -axis and 3 is r -axis.

2.1.1 Orthotropic properties

Composite laminates are anisotropic and, more specifically they have orthotropic properties. This implies that the elastic properties remain the same if the direction perpendicular to the symmetry plane is reversed [12]. Hence, the elastic properties will not be the same in longitudinal, transverse and out-of-plane direction. Nine individual parameters are included in the constitutive relation to model an orthotropic material in Equation (2.1).

$$\begin{bmatrix} \sigma_1 \\ \sigma_2 \\ \sigma_3 \\ \tau_{23} \\ \tau_{13} \\ \tau_{12} \end{bmatrix} = \begin{bmatrix} C_{11} & C_{12} & C_{13} & 0 & 0 & 0 \\ C_{21} & C_{22} & C_{23} & 0 & 0 & 0 \\ C_{31} & C_{32} & C_{33} & 0 & 0 & 0 \\ 0 & 0 & 0 & C_{44} & 0 & 0 \\ 0 & 0 & 0 & 0 & C_{55} & 0 \\ 0 & 0 & 0 & 0 & 0 & C_{66} \end{bmatrix} \begin{bmatrix} \varepsilon_1 \\ \varepsilon_2 \\ \varepsilon_3 \\ \gamma_{23} \\ \gamma_{13} \\ \gamma_{12} \end{bmatrix} \quad (2.1)$$

A more special behavior is the transversely isotropic material which have isotropic properties in the plane orthogonal to the longitudinal direction, hence the properties in the transverse and out-of-plane direction will be the same. This reduces the stiffness matrix in Equation (2.1) to the final Equation (2.2).

$$\begin{bmatrix} \sigma_1 \\ \sigma_2 \\ \sigma_3 \\ \tau_{23} \\ \tau_{13} \\ \tau_{12} \end{bmatrix} = \begin{bmatrix} C_{11} & C_{12} & C_{13} & 0 & 0 & 0 \\ C_{21} & C_{22} & C_{23} & 0 & 0 & 0 \\ C_{31} & C_{32} & C_{33} & 0 & 0 & 0 \\ 0 & 0 & 0 & \frac{C_{22}-C_{23}}{2} & 0 & 0 \\ 0 & 0 & 0 & 0 & C_{66} & 0 \\ 0 & 0 & 0 & 0 & 0 & C_{66} \end{bmatrix} \begin{bmatrix} \varepsilon_1 \\ \varepsilon_2 \\ \varepsilon_3 \\ \gamma_{23} \\ \gamma_{13} \\ \gamma_{12} \end{bmatrix} \quad (2.2)$$

The reduction of the compliance matrix in a transverse isotropic material reduces the unknown material parameters, from nine in the orthotropic case down to five. Determining these five properties provides the basis for design of laminates and is the focus of the following test plan.

2.1.2 Element types in Abaqus

The integration points are points inside the element where the integrals will be numerically solved. When defining a composite lay-up in Abaqus, each solid element will contain the assigned lay-up that can consist of multiple plies. Each ply in the lay-up will have individual integration points, with the default of one point per ply through the thickness for solid elements. Abaqus solid elements require an odd number of integration points and depending on the problem the need of more integration points may occur but for the cost of more computational time. When specifying three or five points, they will distribute evenly through the thickness of each layer with points at both top and bottom surface as shown in Figure 2.2. With a higher amount of integration points, the element will be solved more exactly for non-linear problems but at a higher computational cost.

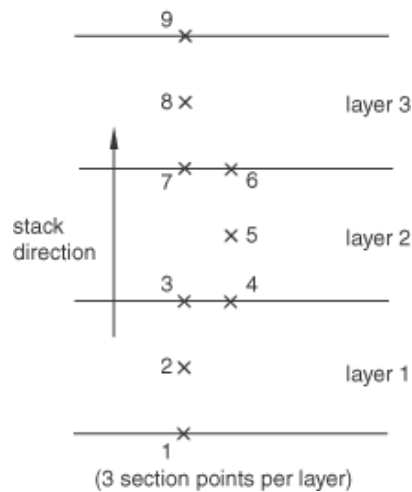


Figure 2.2: Example for a three ply composite with three integration points per layer [1].

2.1.2.1 Eight-noded solid element C3D8

A general purpose eight-node fully integrated brick element [2]. The element is fully integrated with eight integration points as shown in Figure 2.3. Strains and stresses are well captured with these elements but they can suffer from shear locking and are too stiff if subjected to bending due to the numerical formulation of the element [13].

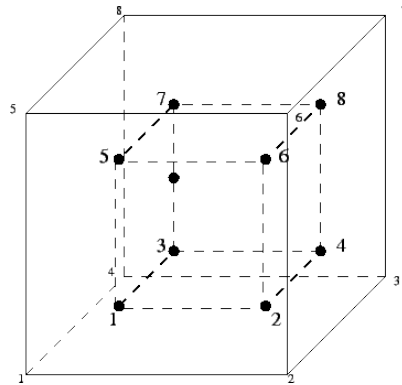


Figure 2.3: C3D8: A general purpose fully integrated eight-node brick element [2].

2.1.2.2 Eight-noded solid element - reduced integration C3D8R

A general purpose eight-node brick element with reduced integration [3]. The element uses reduced integration with one integration point (shown in Figure 2.4) to save computational resources. Due to the single integration point, the element need hourglass control [13] to prevent spurious zero energy modes that may give large and unphysical nodal displacements. With the integration point in the middle, the element size need to be sufficiently small to capture the stress and strain correctly.

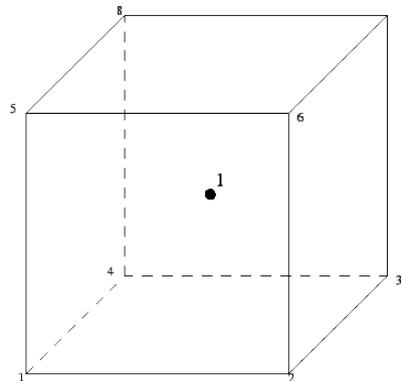


Figure 2.4: C3D8R: A general purpose eight-node brick element with reduced integration [3].

2.1.2.3 Twenty-noded solid element C3D20

A general purpose twenty-node quadratic brick element [4]. The element is fully integrated with 27 integration points as seen in Figure 2.5. Stresses and strains are well captured in elastic behaviour due to the high amount of integration points near the surface of the element. For non-linear behaviour it can have the same problem as the C3D8 element due to the numerical formulation [4].

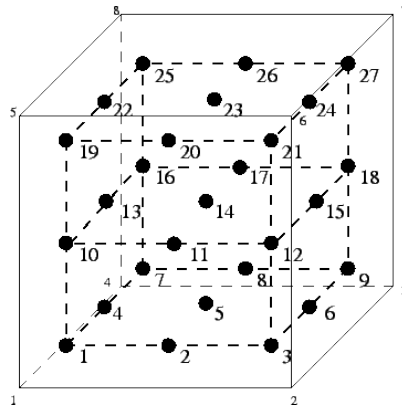


Figure 2.5: C3D20: A general purpose fully integrated twenty-node brick element [4].

2.1.2.4 Twenty-noded solid element - reduced integration C3D20R

A general purpose twenty-node quadratic brick element [14]. The element use reduced integration with eight integration points as seen in Figure 2.6. General purpose element that rarely suffer from hourglassing even though it is formulated with reduced integration. Works well for isochoric (constant volume) material behaviour and when the element is subjected to bending [14].

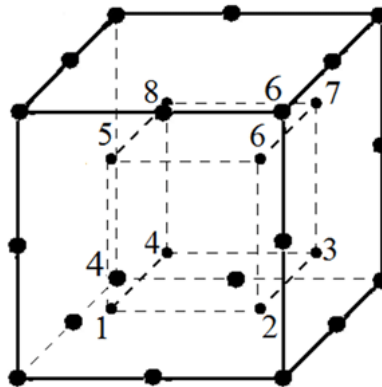


Figure 2.6: C3D20R: A general purpose twenty-node brick element with reduced integration [5].

Based on the available solid elements for composites, all of the elements above (C3D8, C3D8R, C3D20 and C3D20R) were evaluated and compared and the results can be seen in Section 3.2.1

3

Methods

This chapter describes the methodology of the thesis. It includes methods for initial analysis, modeling and building of the test rig, physical testing and characterization of the material properties.

3.1 Choice of lay-ups and material systems

Twelve tubes of four different material systems were provided by *Easton* however, due to the circumstances only ten strain gauges were available. Due to the lack of strain gauges not all the provided material systems were investigated. Instead the three tubes (one material system) in Table 3.1 were selected to proceed with for the initial analysis. The chosen tubes are made of carbon fiber and have the lowest fiber area weight (FAW) of the provided material systems. They are specially chosen to have different lay-ups to give better and more isolated material response in the physical tests.

Table 3.1: Layups for the provided carbon tubes.

Tube label	Fiber orientation
<i>T1</i>	[±80/90/C90]
<i>T2</i>	[0/90]
<i>T3</i>	[±45]

3.2 Choice of physical tests

Based on the classical laminate theory [12], the assumption of transverse isotropic material behaviour and results of the literature study where Gopal [8], Perillo [7] and Kastenmeier [10] who are all using the split hoop test based on ASTM D-2290 [15]. It was estimated that a split hoop test on *T1* would be suitable in order to retrieve the longitudinal data and Poisson ratio while axial compression of the same hoop would be used to retrieve the transverse data. To use the same rings for multiple tests reduces the number of strain gauges needed.

To obtain the shear modulus, initial simulations of the the split hoop test was carried out on tube *T3* which due to the 45° plys would have a shear response in circumferential elongation. As alternative experiments, plate compression ASTM D-2412 [16] on *T1* and pure torsion tests on *T2* were designed and tested in Abaqus [17] since they would omit friction from the testing which in turn would eliminate one source of error. Although it was ultimately decided not to use these, since they would add complexity to the methods of testing and the simulations did not add significant results other than the benefit of omitting friction.

Analyses were carried out in Abaqus to look for sensitivity to fiber directions and which test is most sensitive to each material parameter, in order to propose a suitable order of testing. Initial carbon fiber properties were obtained from an example manufacturer's property data sheet as seen in Table 3.2, estimated epoxy matrix values [18] in Table 3.3. These were combined into the lamina properties in Table 3.4 using the volume fraction corresponding to the FAW provided by Easton and classical laminate theory from Chapter 2 in [12]. All the initial analyses were carried out with the data from Table 3.4.

Table 3.2: Standard modulus carbon fiber data.

	Fiber data	
E_f	230	[GPa]
G_f	95.8	[GPa]
ν_f	0.2	-

Table 3.3: Epoxy matrix data.

	Matrix data	
E_m	3.5	[GPa]
G_m	1.25	[GPa]
ν_m	0.35	-

Table 3.4: Normalized lamina data for initial tests calculated with RoM.

	Laminate data	
E_L	1	[GPa]
E_T	0.13	[GPa]
G_{LT}	0.036	[GPa]
G_{TT}	0.047	[GPa]
ν_{LT}	0.64	-
ν_{TT}	1	-

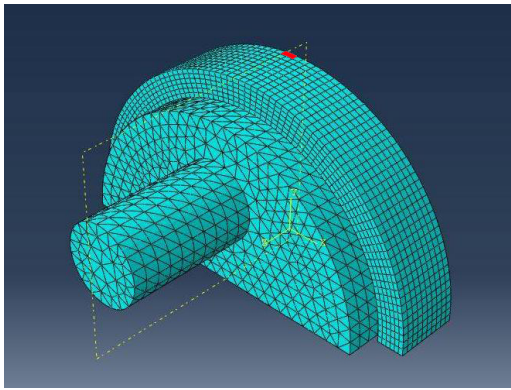
3.2.1 FE model

Since the tubes are produced by a bladder moulding technique[19], the outer diameter is consistent but the inside is rough with inconsistent wall thickness as well as extra epoxy lumps and ridges. Even though the average wall thickness on the chosen tubes are the most consistent of all specimens it still varies over 5 % or approximately 0.1 mm of standard deviation around the circumference while the inner diameter has a standard deviation of approximately 0.15 mm suggesting both lack of concentricity and uneven thickness. Due to the time limit of the thesis, all models were created with a smooth averaged wall thickness.

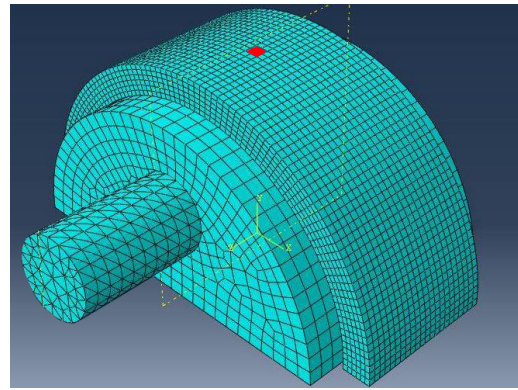
When analyzing this composite geometry in Abaqus, it is not possible to use symmetry boundary conditions due to the issue with mirrored fiber orientations at the symmetry planes. For comparison a quarter (a), half (b) and full (c) model shown in Figure 3.1 is simulated and both longitudinal and axial strains are extracted at the same place near the middle/symmetry line of the models marked in red.

The models are set up with *Hard contact* for the contact interface between the parts since a smooth surface is used of modelling. The alternative would me to model the exact shape of the rings and use a contact pressure curve for the the material interaction. Since the inner surface of the rings are fairly smooth, a contact pressure curve would not add much information. The models are set up with load stepping from 0 – 50 kN which is the range of the physical machine. The load step is carried out with a minimum of ten increments for sufficient resolution of the non-linear area of the results.

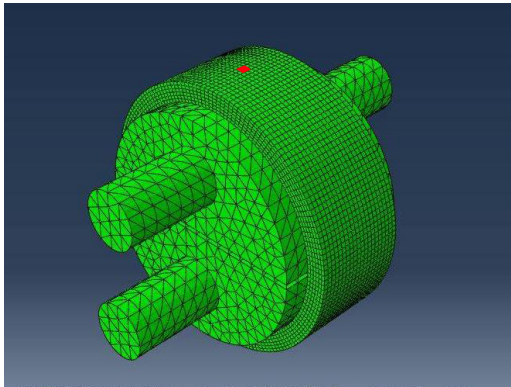
In these and all future simulations an average strain was recorded in a element area which corresponds to an area of the hoop which roughly represents the 1.79×1.79 mm area that the VPG 031WW-350 strain gauges measure [20]. All strains are normalized with the maximum value of the data set range due to the industry collaboration with *Easton*. Furthermore, all strain measures were retrieved from the top integration point of the topmost composite elements in order to simulate surface strain. A method of using membrane shells without any stiffness or thickness on the outer surface of the hoop in order to gather surface strain was tested, however there was no difference in the obtained strains compared to using the outermost integration points. Work was continued with the aforementioned average strains from these integration points.



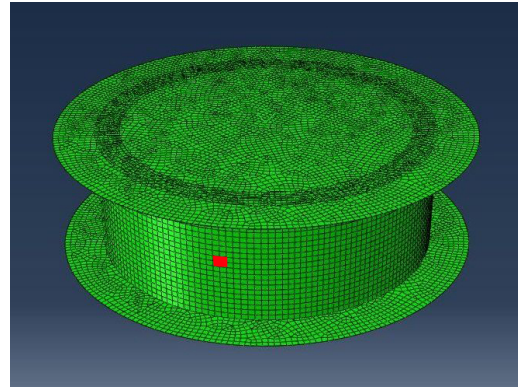
(a) Simulation of quarter split hoop model.



(b) Simulation of half split hoop model.



(c) Simulation of full split hoop model.



(d) Simulation of axial compression model.

Figure 3.1: Initial comparison of different FE models with symmetry boundary conditions and area of strain measurement marked in red.

As seen in Figure 3.2 below the longitudinal response from the full and half model using the split hoop test is quite similar using 20 increments. The simulation on the half model using ten data points showing that it is sufficient enough.

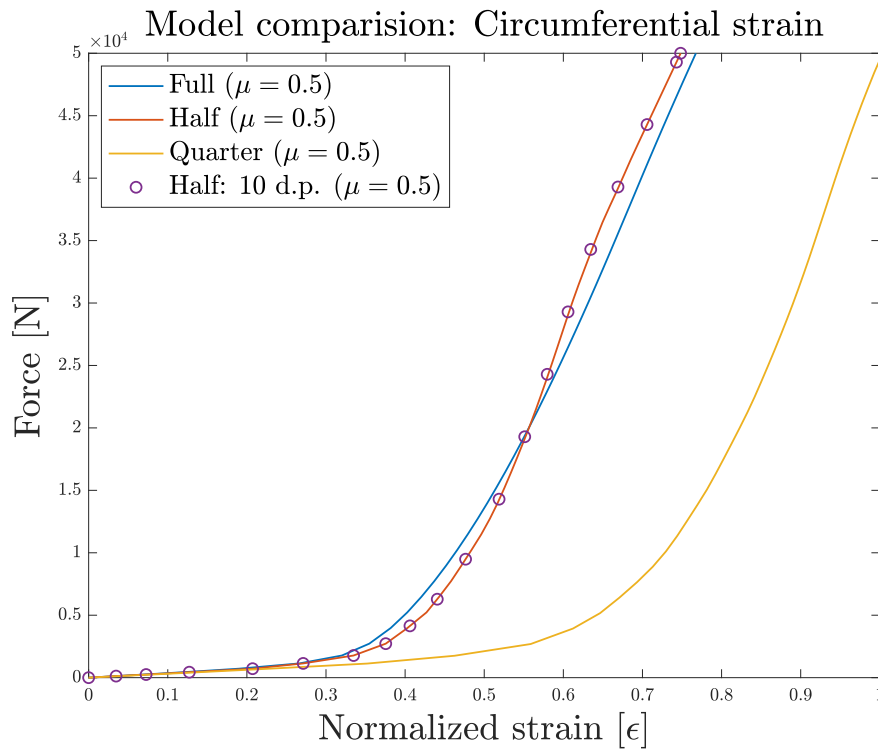


Figure 3.2: Simulated average circumferential strain in the split hoop test for different FE models.

For the axial strain, a noticeable difference is seen between the full model and the half and quarter ones (see in Figure 3.3). This is due to the earlier mentioned symmetry boundary conditions. The computational time for running the full model is around 780 s while the quarter model only took 180 s. Since the strain results vary and the computational cost is reasonable, the decision was made to not further investigate boundary conditions. Therefore the full models with a minimum increment value of ten were used for all simulations to get the most accurate results in both split hoop and axial compression (d).

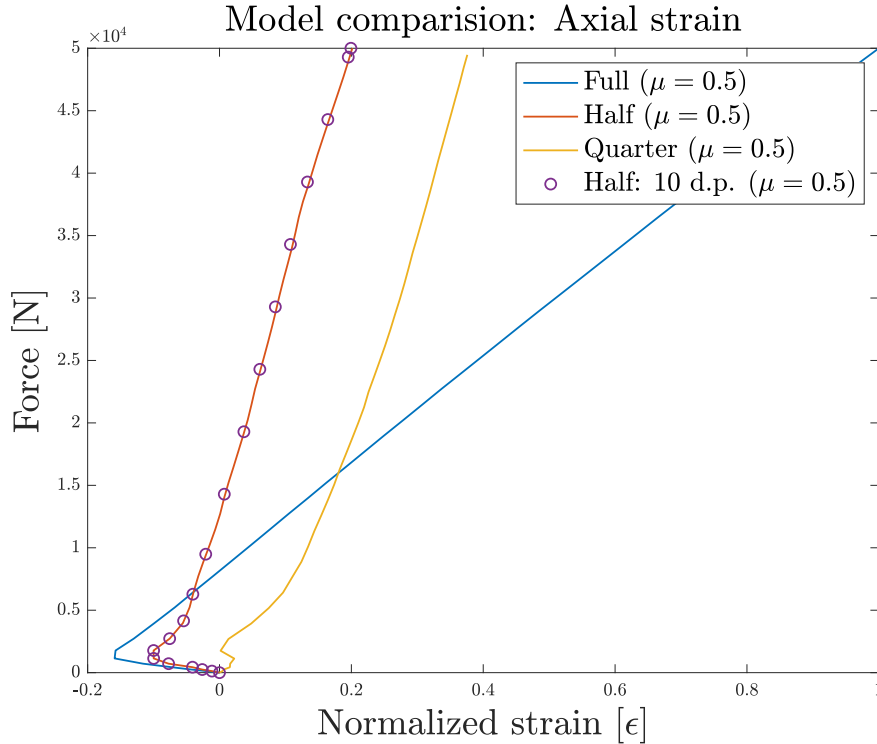


Figure 3.3: Simulated average axial strain in the split hoop test for different FE models.

3.2.2 Mesh dependency

A mesh sensitivity study was carried out on the split hoop test to investigate dependency of mesh size and element type. All simulations were carried out with solid elements which better capture the impact of the out-of-plane strains [21], [22]. Another factor in choosing solid elements was the rough inside surface of the hoops, if it would later be decided to model the shape of the rough inner surface of the rings, this would be easier to do using solid elements. The global size of the composite solid, linear, reduced integration elements (five integration points) was varied between 0.3 – 1.2 mm while the through thickness element size was maintained at 0.25 mm. This is due to the fact that Abaqus applies the composite layup once in each element in order to specify the composite layup [23]. This study showed a difference in average strain measurements of 1.2 % which was not headed in any specific direction but shows a v-shaped curve, instead the major difference was computational time which increased from 9 m to 9 h. Hence all further simulations were carried out with a in-plane global size of 0.9 mm which was roughly at the center of the strain range. A full presentation of the mesh dependency can be seen below in Table 3.5 and Figure 3.4

Table 3.5: Table showing element values and computational time from mesh sensitivity study

Global Size [mm]	Aspect Ratio	CPU Time [min]
1.2	4.8	9
0.9	3.6	13
0.7	2.8	20
0.5	2	45
0.3	1.2	540

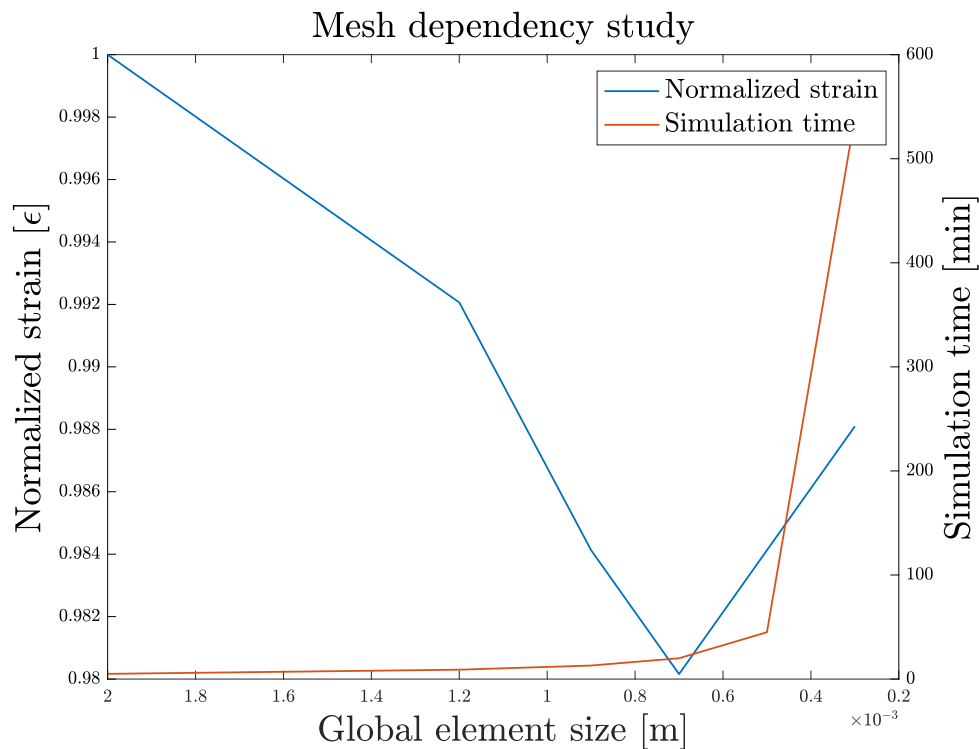


Figure 3.4: Figure showing mesh dependency study for split hoop test based on global element size and circumferential strain.

The mesh dependency for compression showed a similar behavior (Figure 3.5) where the largest difference in strain was approximately 4 %. Again, no clear direction was found in the curve and 0.9 mm global mesh size was chosen to match the split hoop model for modelling convenience.

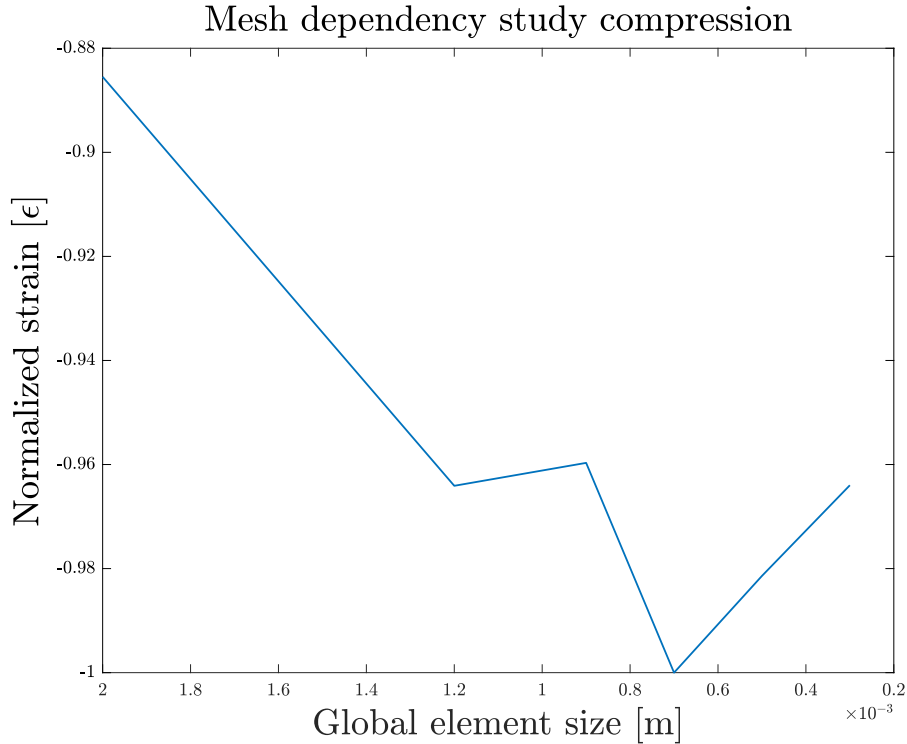


Figure 3.5: Figure showing mesh dependency study for axial compression test based on global element size and axial strain.

Additionally four different types of standard elements were tested for the split hoop simulation. The previously mentioned reduced integration linear solid element which is standard in Abaqus linear static analysis was used as a baseline and tested against: full integration linear, reduced integration quad and full integration quad; all of which are described in further detail in Section 2.1.2. The same split hoop simulation as in the mesh dependency study was set up with the different element types and the results showed a maximum divergence from the baseline of 0.002 % which again was deemed not to be of enough significance to motivate the added computational time. Hence, the cheapest computational element C3D8R was chosen for further simulations.

3.2.3 Analysis of axial compression test

In the FE analysis of the axial compression case it was found that the minimum width of each specimen had to be 20 mm to avoid edge effects and to get consistent strain measurements on the area where the strain gauges were placed as seen in Figure 3.6. The width was kept to a minimum to suit both axial compression and split hoop tests on the same specimen, as mentioned in Section 3.2. The minimum width of specimen that is needed for the axial compression alters the range of measurement in the split hoop test as discussed below in Section 3.2.4.

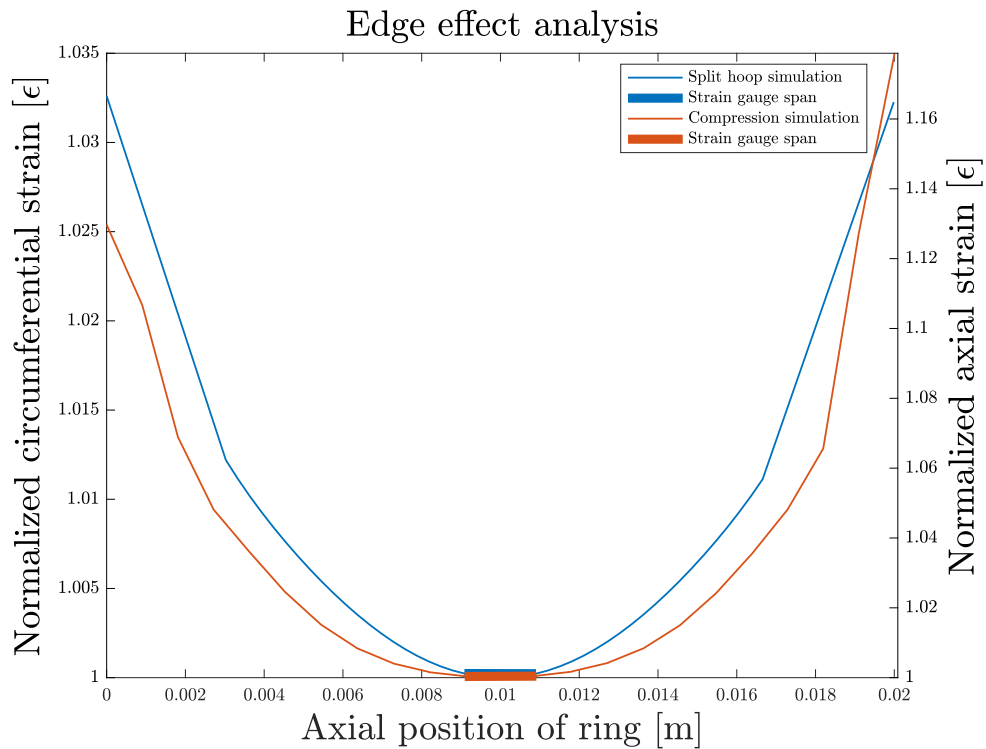


Figure 3.6: Figure showing show axial and circumferential strains vary across the hoops, showing edge effects.

For a set compressive force of 50 kN, the influence on the maximum average axial strain with respect to different ν_{LT} and E_L will be analyzed. As shown in Figure 3.7 and Figure 3.8, both the longitudinal stiffness and Poisson ratio had very little effect on transverse stiffness of the rings. With fixed values of E_T and E_L and varying ν_{LT} between 0.2 – 0.4 based on common carbon fiber and epoxy data [24], [25], the axial strain for the highest and lowest value gives a negligible difference as seen in Figure 3.7.

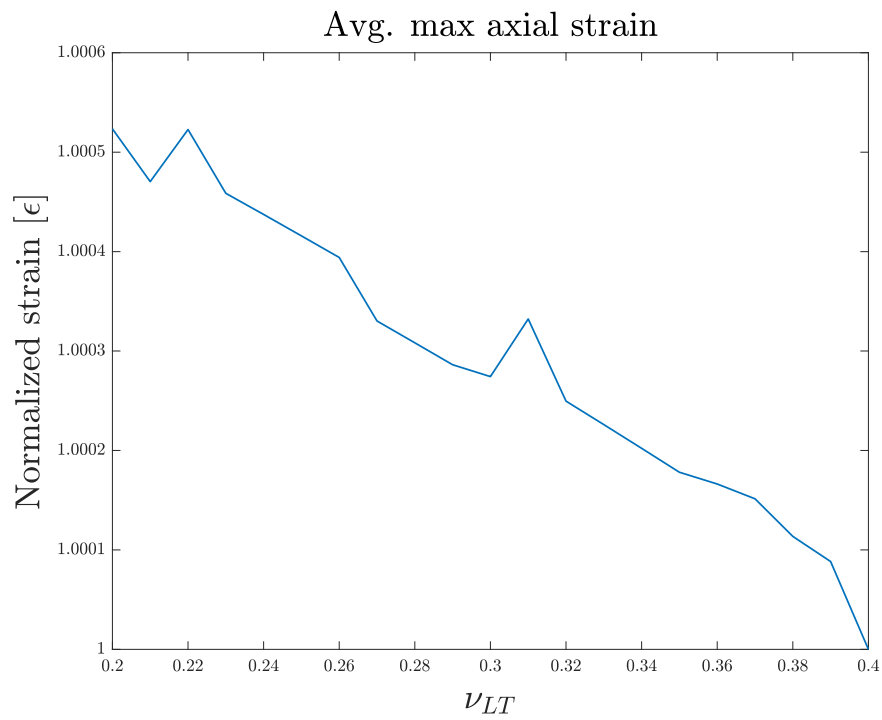


Figure 3.7: Sensitivity of average maximum axial strain due to different ν_{LT} in axial compression.

Using the same procedure but varying E_L between 100 – 300 GPa, the difference in the maximum averaged axial strain is approximately 2 % as seen in Figure 3.8.

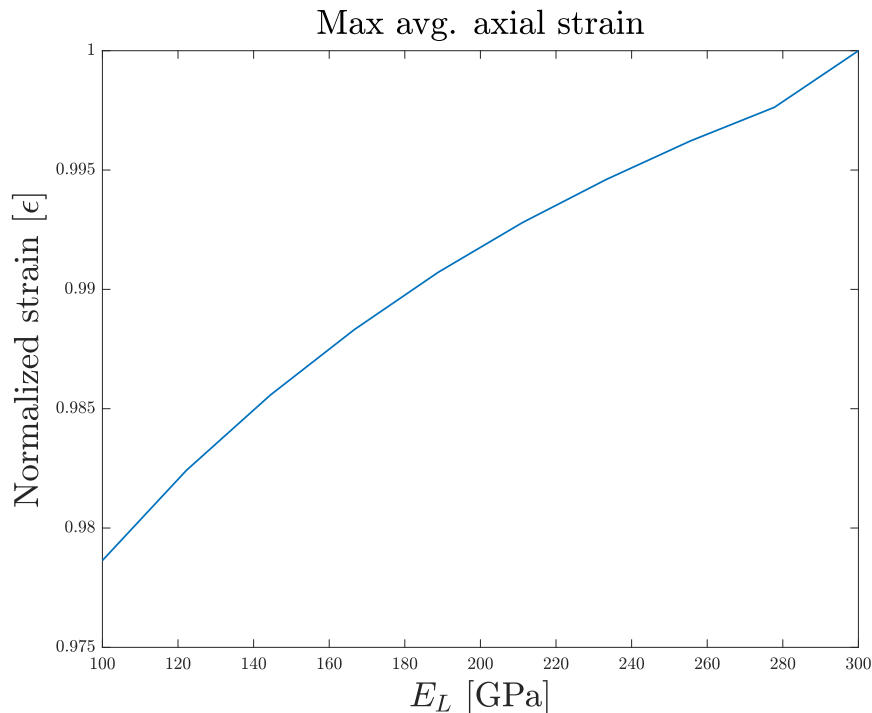


Figure 3.8: Sensitivity on the maximum averaged axial strain with respect to different E_L in axial compression.

With commonly used friction coefficients for polymers [26] and a study within carbon fiber epoxy against steel [27], the assumed range of friction coefficient between the specimen and steel pucks is $\mu = 0.1 - 0.65$. Varying μ in the simulations for a range of $0.1 - 0.65$ showed small differences 2.73% in the force/strain response between the highest and lowest coefficient of friction. Even though friction had a small effect on the compression simulations it was decided to be significant enough to include friction in the simulations. The frictional effects in compression are believed to cause a phenomenon called barrelling where the boundaries' radial movement is restricted by friction and hence a difference in radial expansion (circumferential strain) is noticed between the center of the specimen and the boundaries.

Due to the fact that it is hard to manufacture rings with only 90° fibers, the rings have some $\pm 80^\circ$ layers to hold them together that could have influence on the transverse stiffness. In the axial compression test, the force response for a given displacement between the 60° and 90° layers are constant as seen in Figure 3.9. Hence, the influence on E_T by the $\pm 80^\circ$ layers are negligible. This is also handled directly in Abaqus since it is defined in the composite layup. As the angle is getting closer to 45° it will have a higher influence on the transverse stiffness which also can be seen in Figure 3.9 below [28].

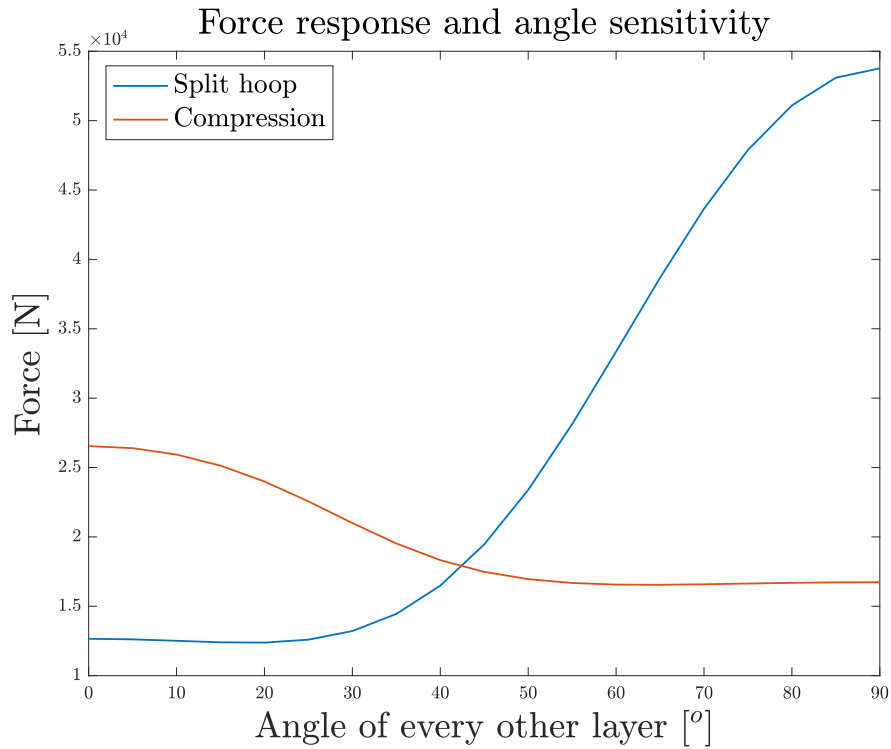


Figure 3.9: Force response for a set displacement with changed ply orientations on tube *T1*. The angle is measured from the axial direction on the tube.

Since there is small angle between the 80° and 90° layer it was assumed that the in-plane shear modulus G_{LT} would not have a significant effect when extracting the transverse stiffness. The out-of-plane elastic properties was also assumed negligible due to the relatively thin geometry of the tubes. Hence the axial compression test was deemed suitable as a first test since the transverse stiffness was more or less isolated as the main driver of the axial strain response.

3.2.4 Analysis of split hoop test

The same directional and frictional sensitivity studies were carried out for the split hoop test of tube $T1$. These simulations showed that E_T had more influence on hoop stiffness in the split hoop test than E_L had on axial stiffness in compression. It turned out to be 1.7 % difference on the circumferential strain with E_T in the range of 10 – 20 GPa which can be seen in Figure 3.10 below.

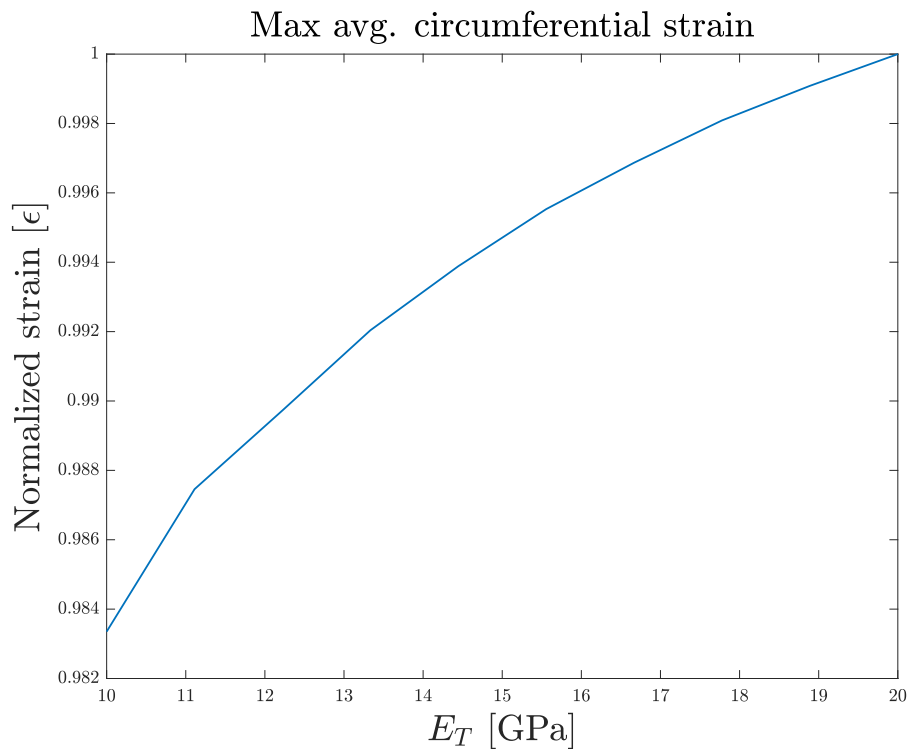


Figure 3.10: Sensitivity on circumferential strain with respect to different E_T in split hoop test.

In the case of isolating the longitudinal stiffness E_L , the Poisson ratio did not show much influence at all on the maximum average circumferential strain. With fixed E_L and E_T and varying ν_{LT} from 0.2 – 0.4 as in the compression case, the difference in circumferential strain is less than 0.15 % in the whole linear region as seen in Figure 3.11.

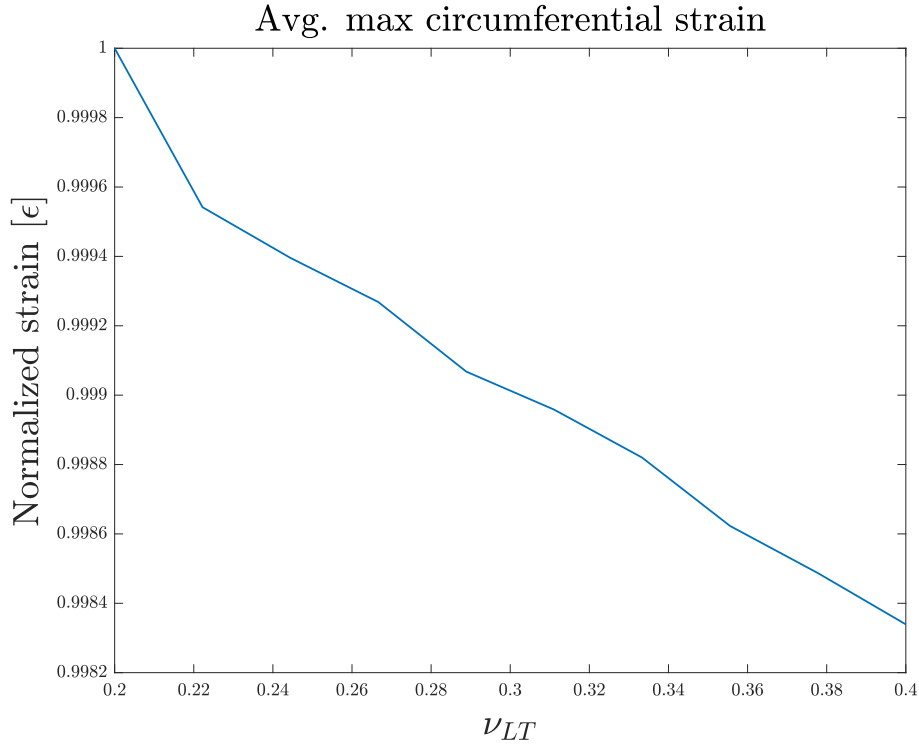


Figure 3.11: Sensitivity on circumferential strain with respect to different ν_{LT} in split hoop test.

Since half of the layers in $T1$ are offset by 10° from the circumferential direction of the hoop, a potential source of error presents itself and a simulation of angular direction in the non 90° plies were conducted in the same manner as for the axial compression test. It showed that difference in force response for a set displacement was 5 % between 80° and 90° as seen in Figure 3.9 [28].

For the split hoop tests, the friction coefficient plays a major role for the circumferential strains. At peak load of 50 kN gives that circumferential strain will differ 23 % between frictionless and having the friction coefficient $\mu = 0.5$. The curves also show a different behavior through the load range as seen in Figure 3.12 below where the higher coefficients of friction show a more non-linear response. Studies have shown that the friction coefficient between metal and carbon fiber epoxy may vary from 0.1 to 0.65 depending on the initial conditions [27]. As the surface finish on the rig will be machined steel and the inside of the hoops are uneven with carbon and epoxy, the initial friction coefficient for all future simulations is set to $\mu = 0.5$.

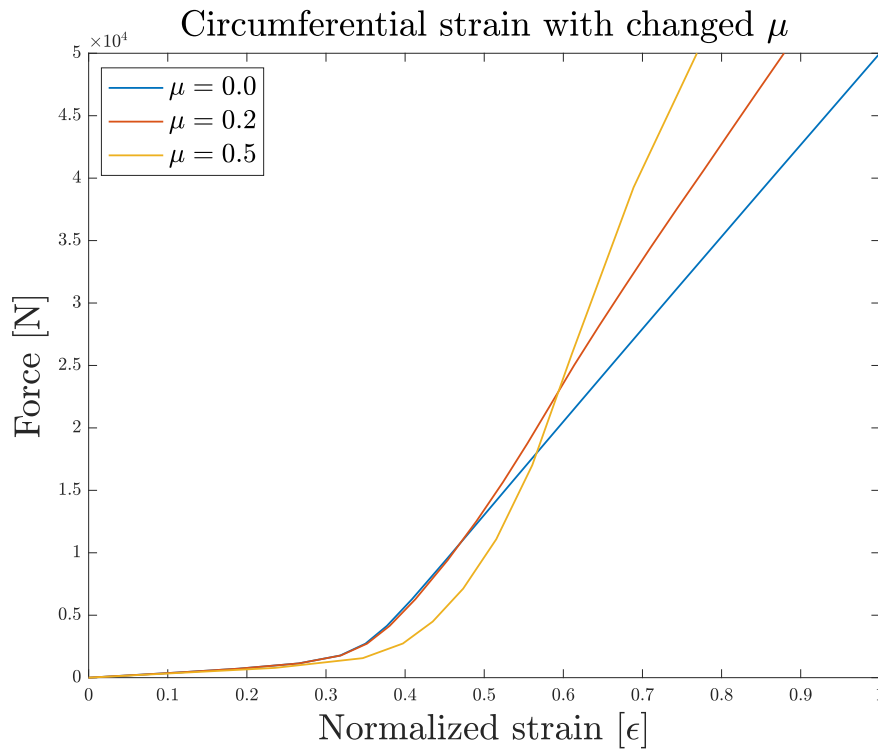


Figure 3.12: Sensitivity on circumferential strain with respect to different friction coefficient μ in split hoop test.

In the axial compression case with fixed E_L and E_T , different Poisson ratios will have a great affect on the circumferential strain. A small change in ν_{LT} changes the averaged circumferential strain a lot as seen in Figure 3.13 below. Simulations show that determination of ν_{LT} in compression is sensitive and dependent on the previously determined longitudinal modulus E_L .

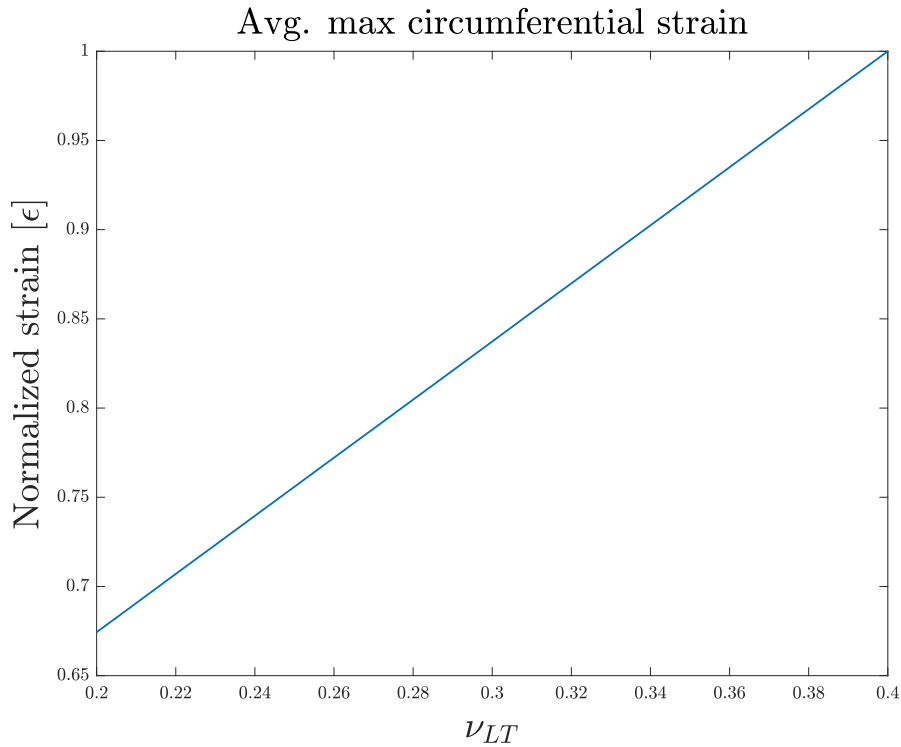


Figure 3.13: Sensitivity on the averaged maximum circumferential strain with respect to different ν_{LT} in axial compression.

Even though the axial strain of the split hoop simulation shows a lower sensitivity to a change in Poisson's ratio compared to how the circumferential strain changes over the same Poisson's ratio range in the axial compression simulation (see Figure 3.14) it was decided to proceed with the split hoop test to determine the Poisson's ratio since the other elastic properties had a lower relative effect on axial strain. For example the non primary modulus E_L affects circumferential strain in axial compression more than the non primary modulus of the split hoop simulations E_T affects the axial compression of the split hoop simulation. Furthermore, in compression the epoxy needs to expand against the stiffness of the fibers while in tension it is mostly the epoxy that is contracting and at the same time contracting the fibers in their weaker transverse direction. The one thing that is working against using the split hoop for extracting ν_{LT} is the presence of friction which was shown in Section 3.2.4 to have less effect compression. The conclusion was however, that the benefits of the split hoop test outweighed the influence of friction and it was decided that the split hoop test should be used to extract ν_{LT} .

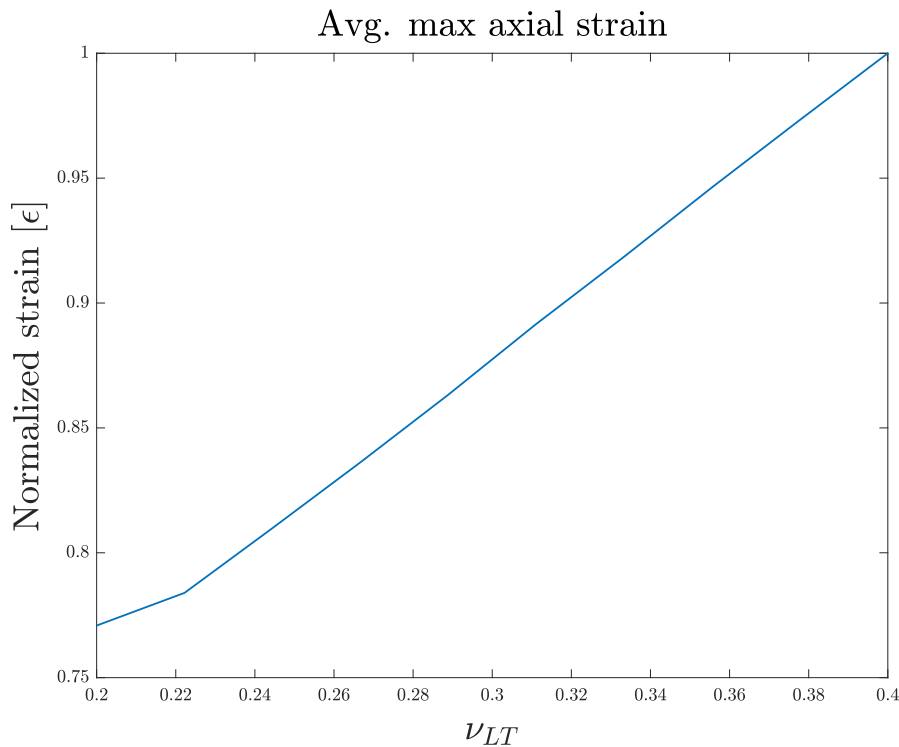


Figure 3.14: Sensitivity on the averaged maximum axial strain with respect to different ν_{LT} in the split hoop test.

3.2.5 In-plane shear modulus

To determine the suitability of the split hoop test for extracting the shear modulus G_{LT} , simulations on tube $T3$ were conducted with different E_L , E_T and ν_{LT} in order to determine the sensitivity of the test would be. The maximum average circumferential strain was measured with respect to the changes on the different parameters. Due to the layup on tube $T3$, the circumferential strain should mainly be a response from the shear modulus. Changing the longitudinal stiffness E_L between 100 – 300 GPa made a 10 % difference on the circumferential strain on the whole range as seen in Figure 3.15 below. From initial RoM calculations and the carbon fiber data sheet, assuming that the range of E_L is between 120 – 180 GPa the variation in circumferential strain will be around 4 %. Changing the transverse stiffness E_T between 10–20 GPa made less than 1 % difference on the circumferential strain.

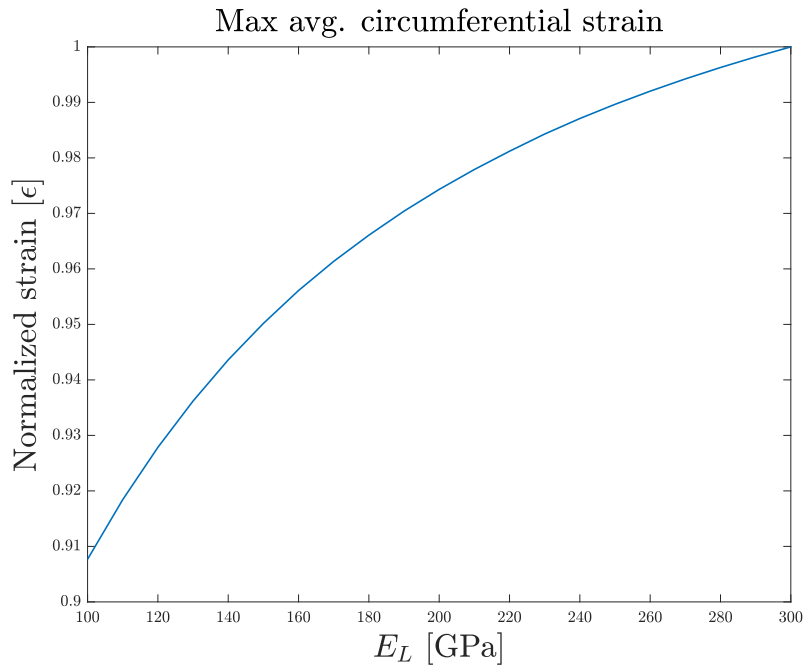


Figure 3.15: Averaged maximum circumferential strain when varying E_L on tube $T3$ in the split hoop test.

While keeping parameters E_L , E_T and G_{LT} fixed and varying ν_{LT} , the circumferential strain changes approximately 1 % as seen in Figure 3.16. Hence the determination of the shear modulus G_{LT} appears insensitive with respect to the Poisson’s ratio.

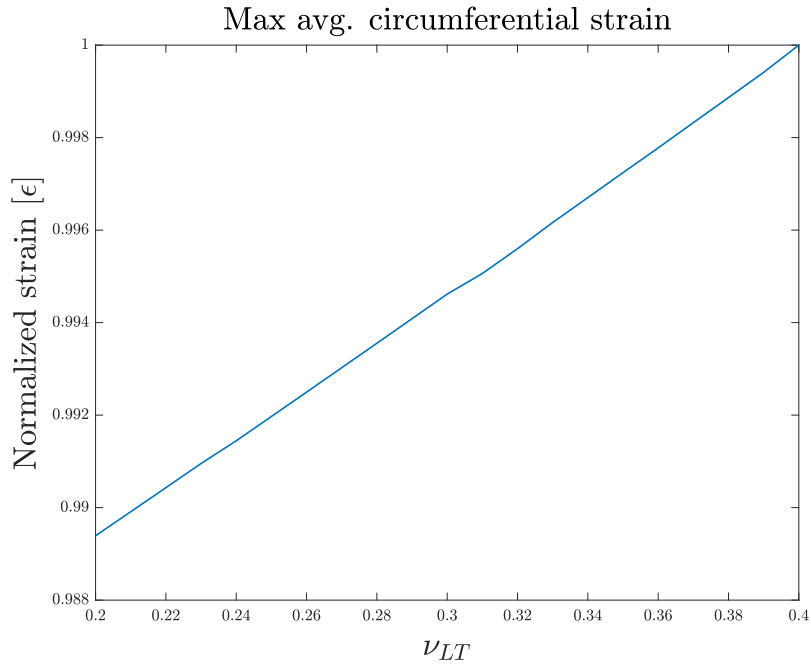


Figure 3.16: Averaged maximum circumferential stress when varying ν_{LT} on tube $T3$ in the split hoop test.

With fixed values on E_L , E_T and ν_{LT} it can be shown that both the circumferential and axial strain are highly dependent on the shear modulus. When varying G_{LT} between 3 – 8 GPa, the circumferential strain differs 240 % as seen in Figure 3.17 below. Initial simulations then show that the evaluation of the shear modulus is then independent from the other parameters.

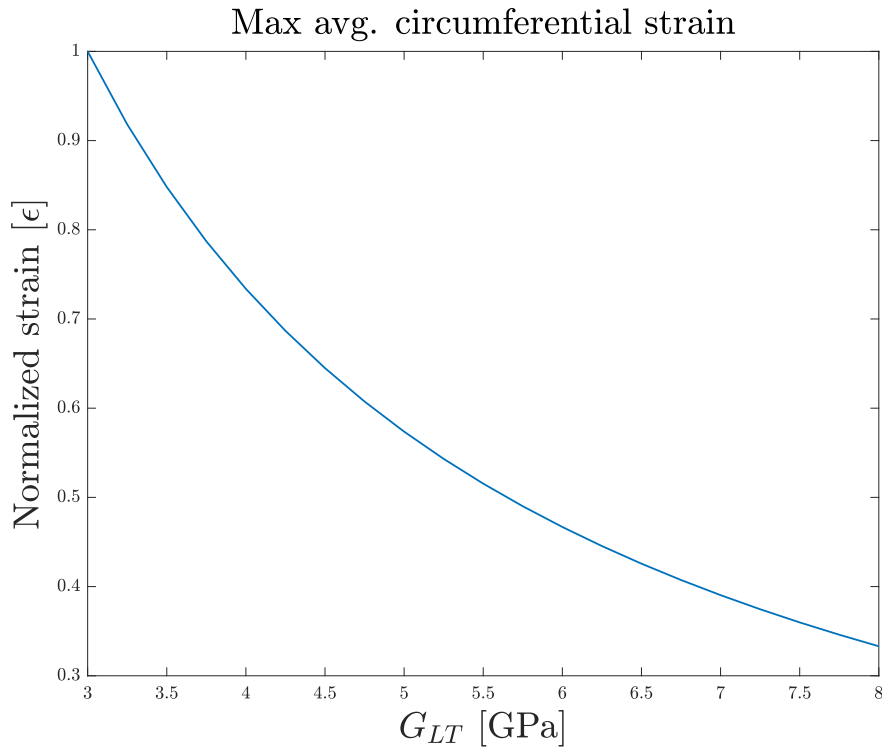


Figure 3.17: Averaged maximum circumferential stress when varying G_{LT} on tube $T3$

3.3 Modeling of the test rigs

The split hoop rig which can be seen in Figure 3.18 was designed with inspiration from ASTM D-2290 [15] although some parts were altered for ease of use and strengthening of the rig. The pucks were modelled to be milled from a solid piece of steel in order to further strengthen the interface between the pucks and the plates instead of the loose pin solution used in ASTM D-2290 since play between pucks and axles is eliminated. Furthermore this solution would further reduce the possibility of transverse motion of the pucks during testing. Due to the rough surface of the inner specimen diameter created by the bladder moulding process the puck diameter was reduced by 1 mm compared to the average inner diameter of the specimen in order to fit the specimen onto the pucks for testing. The 12 mm pins at the top and bottom of the rig were part of the tensile test machine interface and a part of why the rig was redesigned from the ASTM D-2290 drawing.

3. Methods

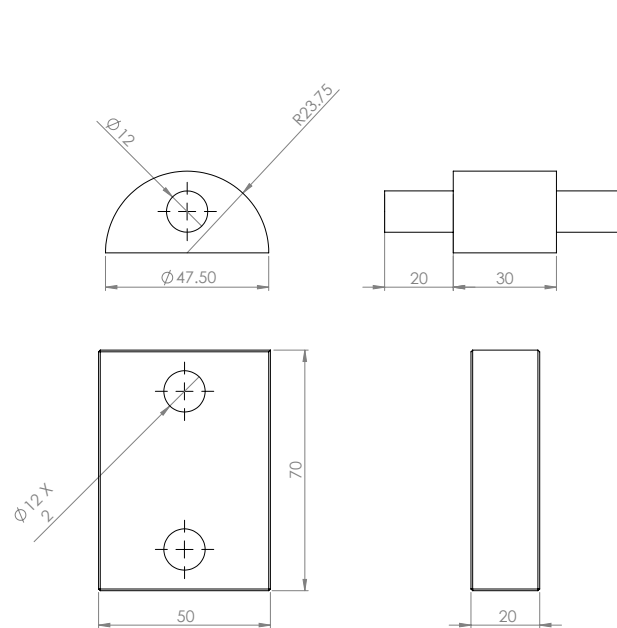


Figure 3.18: Drawing of the split hoop rig used for testing

The split hoop rig was modeled entirely in Abaqus in order to make sure that the rig would not reach yield stress anywhere and break or see excessive deformation around the pin areas. The models showed high stress areas around the pins, however the areas were very small and there was nothing in the results to suggest rig failure would occur.

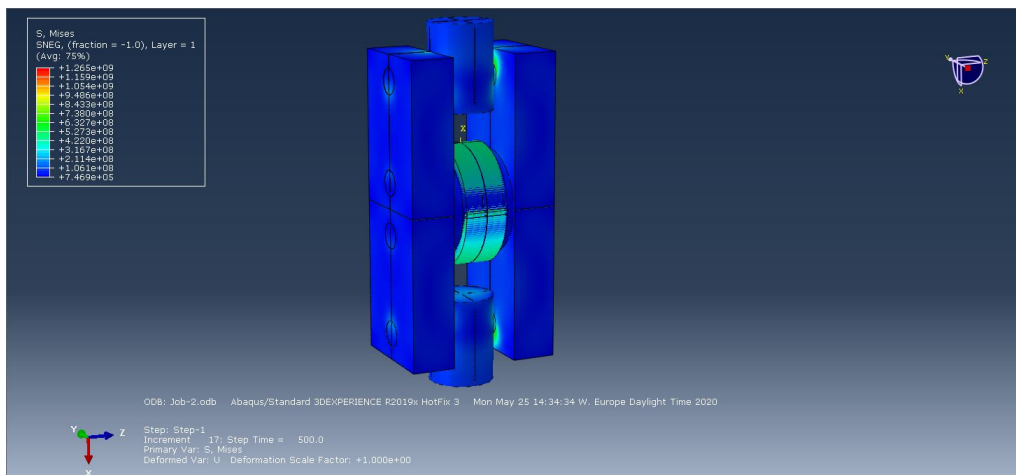


Figure 3.19: Figure showing the stress distribution in the rig, with hot spots at the pin-plate interface

No modelling was done for the compression test since it used very thick cylinders (Figure 3.20). Dividing the maximum force of the machine with the cross sectional area of the rings(normal to the axial direction) showed a rough stress calculation of 70 MPa which is well within limits of operation for carbon steel.

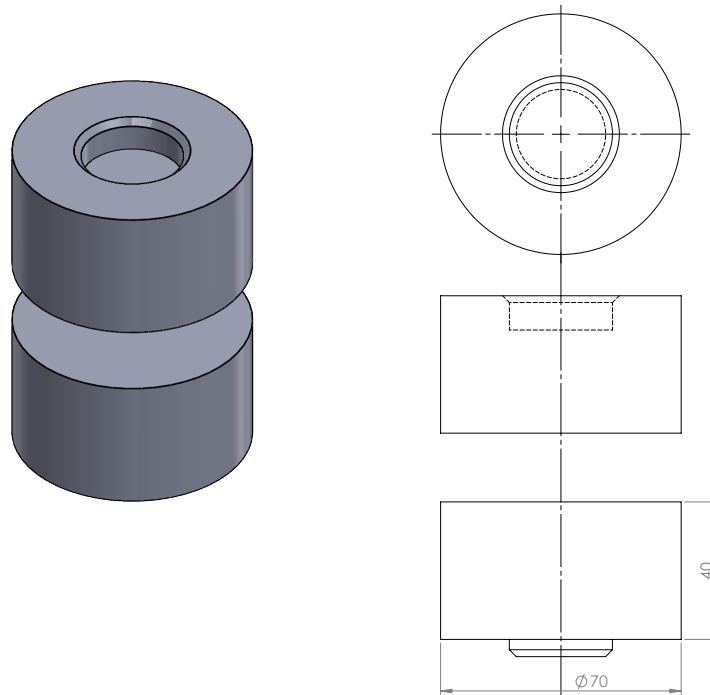


Figure 3.20: Drawings of the compression test rig used for testing

3.4 Building of rig

The rig was constructed by readily available carbon steel stock material (S235JR) for ease of construction. The pucks were milled from 70 mm round stock in order to add some strength, stiffness and stability to the assembly. These benefits come from the fact that no hole/pin interface exists between the pucks and pins which also has the benefit of restricting transverse motion of the pucks, however a loose pin construction like the one in ASTM D-2290 [15] would be a sufficient method of construction if machine shop access is limited since it does not change the function of the rig in any way. The plates holding the rig together were made from hot rolled 50x20 mm S235JR steel bar.

The axial compression test rig was turned from 70 mm diameter carbon steel round stock into 40 mm tall cylinders with has a counter bore at the top and a locating pin at the bottom to receive the vertical axle and threads from the tension test machine in order to ensure proper alignment.

3.5 Preparing samples

The $T1$ and $T3$ carbon tubes were cut to width of 20 mm in a diamond wheel, water cooled table saw for a good surface finish and parallel cuts. The rings were measured again and sanded on a glass plate covered with 240 grit sand paper to ensure the sides were flat and parallel. They were measured again on a surface plate for both width and parallelism, both of which was within the 1 % range of nominal values. All rings were labeled with the tube label $T1$ or $T3$ and with the sub index of a capital letter A-J. Before gluing of strain gauges commenced a course in application and use of strain gauges and measuring equipment was attended with the equipment provider to make sure correct procedure was followed.

After proper cleaning with a mild electronics cleaner, a 40 mm long area was sanded on each specimen with P240 grit sand paper to ensure mechanical bonding of an initial layer of the M-Bond AE-10 two component glue [29]. After sanding, some pin holes which can be seen in Figure 3.21a were detected in the surface of some of the specimens. However the thin film of AE-10 applied, filled these holes and made for a smooth homogeneous surface shown in Figure 3.21b for the strain gauges to be adhered to. After AE-10 was applied the specimen were cured at 50°C for 24 h in order to ensure sufficient stability in the glue [29].



(a) Picture showing pinholes which occurred in some specimen



(b) Picture of Surface prepared with cured AE10 glue.

Figure 3.21: Pictures of hoop surfaces during surface preparation.

When the glue had cured for 24 h the surface was again sanded with P240 grid sand paper and cleaned thoroughly to ensure a good bond between the strain gauges and the now homogeneous surface of the specimen. With all surfaces cleaned and dried the strain gauges were catalyzed with M-Bond 200 catalyst [30] for a more controlled adhesive reactivity rate which makes for a strong and predictive bond. After the strain gauges were catalyzed, M-Bond 200 was applied and the strain gauges were adhered to the specimen and covered with protective tape. The final mounting is seen in Figure 3.22

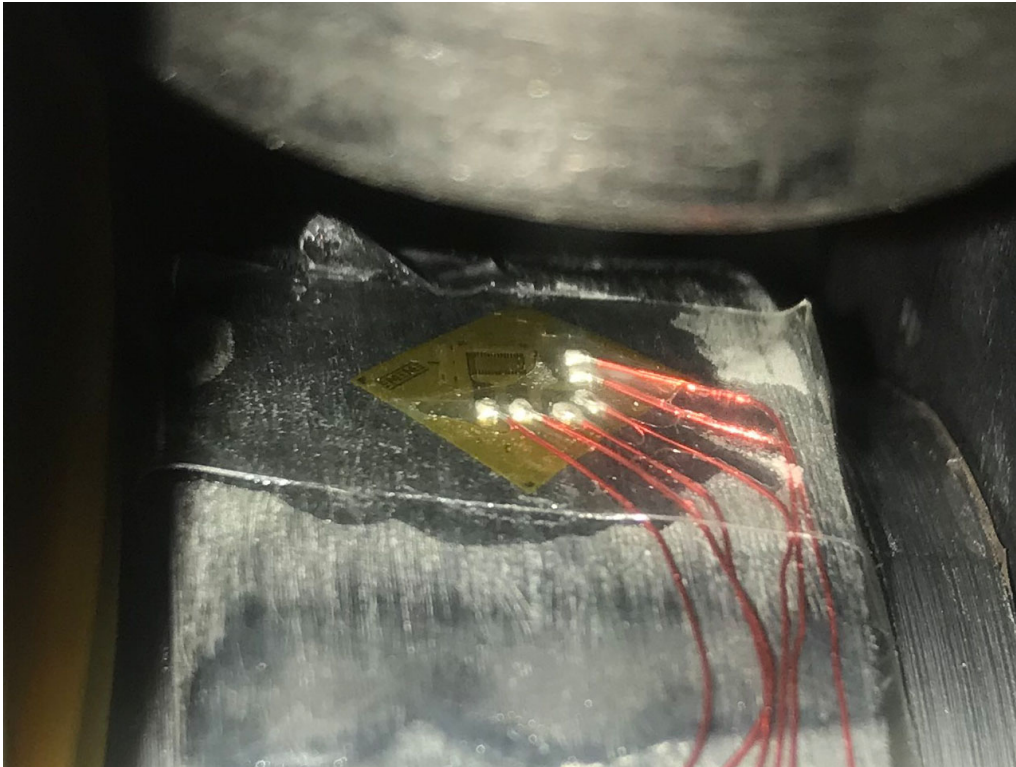


Figure 3.22: Picture showing a strain gauge mounted on a hoop.

3.6 Physical testing

Physical testing was performed with the two tests discussed in Section 3.2; split hoop shown in Figure 3.23 and axial compression shown in Figure 3.24. All testing was performed in a calibrated Bent Tram UCT50 [31] universal compression and tension testing machine. Since the actual strain rate was uncertain due to the material properties and machine flexion being unknown, a displacement rate of 0.5 mm/min was used to ensure that all tests would be quasi-static and to safeguard against any strain rate dependent effects in the material without having to change the speed of the machine between tests. From Figure 3.12, one can see that the rings will conform and bend around the pucks in the split hoop test and hence create a bending moment at the top where the strain gauge is placed which presents itself as nonlinear behaviour with a low slope at the beginning of the load range from 0 – 1 kN where large strain deformation caused by a small load can be seen. Hence a preload of 1 kN was decided as the start point for the test results.

The original plan was to release the load at the same rate as it was originally applied in order to visualize the load/strain curve in both directions and hence see the effect of friction and hence be able to cancel or counter it in later data analysis a method which was later found to have been proposed by Yoon [32]. This however proved impossible with the current software update installed in the tension test machine so friction had to be accounted for in the analysis as discussed in Section 3.2.3.

3. Methods

Strain gauge placement was also investigated and the idea was to place the strain gauge at 12 o' clock (referring to the position on the specimen with reference to the numbers on a clock) in order to distance the gauge from the bending moment which appears between the pucks at 6 and 9 o' clock. This idea was also tested and supported by Yoon[32].

For data collection a LORD V-link 200 [33] was used together with the aforementioned strain gauges. In order to easily sync the data from the built-in load cell of the machine with the third party V-link, a bridge connector was created so that the V-link could capture force data which otherwise is only possible to capture through the tensile test machine software. Additionally, an extensometer was added to the system to measure puck displacement as seen in Figure 3.23. However, placement options were limited and in the end this setup was proven to not be accurate enough considering the flexing of the pins in the split hoop rig, therefore data from the extensometer was later omitted from the results.

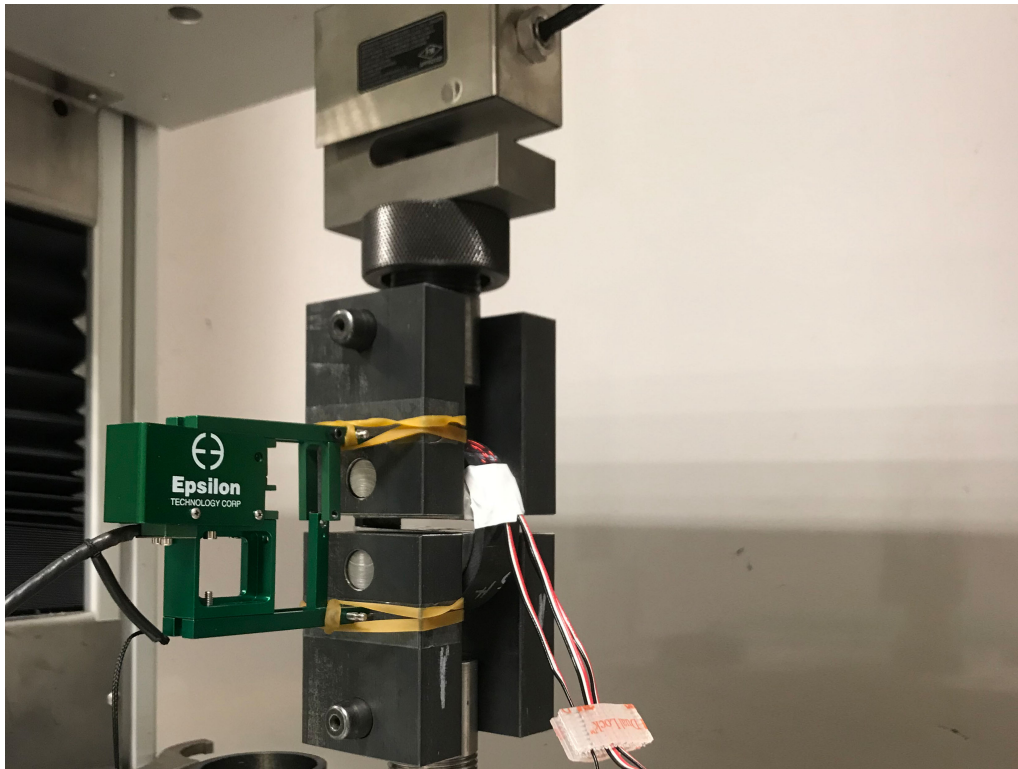


Figure 3.23: Picture showing the split hoop setup and extensometer placing.

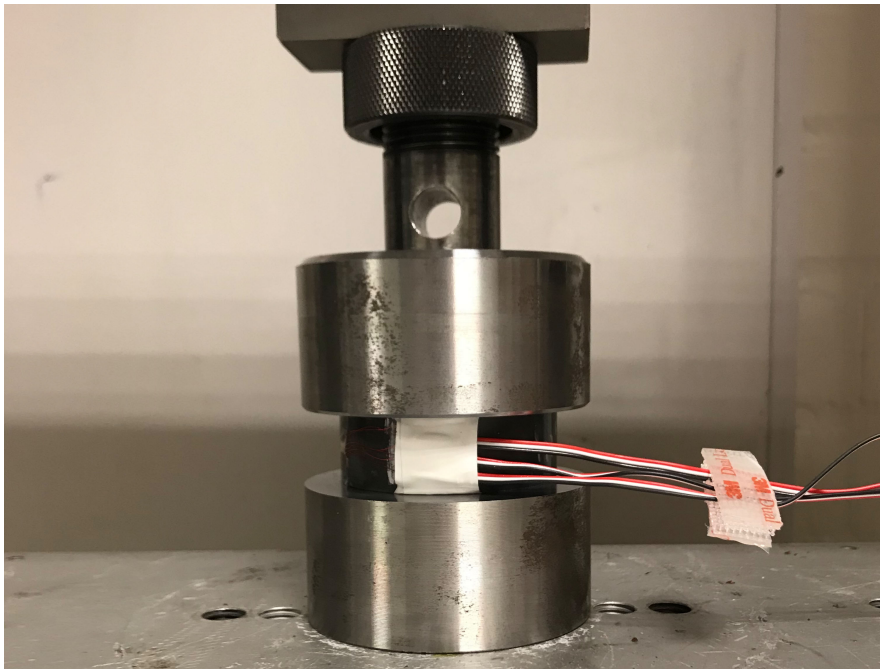


Figure 3.24: Picture showing axial compression test.

In Section 3.3 some local plasticity was discussed at the stress concentration areas of where the pins attach to the pucks. This observation was also made on the actual pucks after all tests were performed, as seen in Figure 3.25. The estimated angle change was approximately 2° and no structural issues were observed. Through visual inspection, all other parts of the rig looked to be in their original shape and there were no signs of loss of structural integrity anywhere.



Figure 3.25: Picture showing the angular deformation of the pins in the split hoop fixture.

3.7 Data handling

The main goal of this thesis was to create a method for finding the elastic in-plane material properties of the material, hence it was chosen to look at the *apparent stiffness*, studying the linear parts of the force-strain curves at the location of the strain gauges rather than absolute strain values. That is due to the possible non-linear effects caused by bending and conforming the slightly larger specimen to the pucks and slightly rough inside of the tubes could skew the data.

All the collected data from the LORD V-link 200 was exported to MATLAB for further analyses. Since the number of tests are limited due to cost, statistical significance of the test data is hard to determine. The ASTM D-2290 standard states that a minimum of five tests is accepted.

In the first step, the data was visually inspected and suspected outliers were removed. Thereafter, a determination of the test results rangewise linearity was performed with a R^2 -value for load ranges of 10 kN. Starting from 0 kN with 5 kN incremental increases, the linearity for each specimen curve and load range was determined. Each load range overlapped the previous by half to ensure that no area was neglected. The R^2 -values for all curves in the same load range were summed up and the load range with the highest sum was considered the most linear. When the load range with the highest combined R^2 had been determined, the mean value from all curves was calculated and a linear slope over the 10 kN area was calculated for use in the upcoming material characterization.

3.8 Material characterization

A general optimizing function in MATLAB called *fminsearch* [34] was chosen, which utilizes the Nelder-Mead algorithm since it can handle many different problem setups due to it not requiring an error function gradient to operate as compared to for example *fmincon* [35]. Since Abaqus can utilize Python [36] for scripting and running with no GUI, MATLAB calls on and collects force and strain data. From this data a force/strain slope is calculated and compared to the corresponding slope data from the physical tests from Section 3.7 with a least square error function. *Fminsearch* then optimizes the chosen material parameter against the least square error until it satisfies the set tolerances presented in Table 3.6. The setting *TolFun* is the increment tolerance for the least square error function discussed above. *TolX* is the tolerance setting for increment size of the input parameters in *fminsearch*.

Table 3.6: List of tolerances used in *fminsearch*.

Parameter	TolFun	TolX
E_L	$1e - 4$	0.1 GPa
E_T	$1e - 4$	0.1 GPa
G_{LT}	$1e - 4$	0.1 GPa
ν_{LT}	$1e - 4$	0.001

As mentioned in Section 3.2 it was shown that the easiest way to go about finding the in-plane material parameters was to try and isolate them one by one. Since the axial compression simulations of $T1$ showed that the transverse stiffness E_T was more or less isolated in affecting the axial strain made it suitable for a first parameter fitting. The least squared error between simulated and measured axial force/strain slope was set as the error function for *fminsearch* to calibrate E_T .

When the transverse stiffness E_T was established the longitudinal stiffness E_L was the next task at hand. Again the introductory simulations in Section 3.2 showed that the influential parameters of circumferential strain in the split hoop test were E_L and E_T , and with E_T already established E_L remained the only driver of circumferential strain and was therefore calibrated second step. As a third step, the Poisson's ratio ν_{LT} was defined. From Subsection 3.2.4 it was found that the axial strain of the split hoop test was highly dependent of E_T and ν_{LT} , and with E_T already established ν_{LT} was the only driver left and could therefore be calibrated. However, when all physical tests were analyzed in Subsection 3.7 it was later seen that the axial strain results from the split hoop test shown in Figure 4.9 was highly inconsistent and non-linear. Hence it was decided to also try to extract ν_{LT} from axial compression which had a more consistent and linear force-strain response.

Finally the shear modulus G_{LT} was established via the $T3$ tubes since it was shown in Section 3.2 that the circumferential strain was highly dependant on E_L and G_{LT} in the split hoop test, and with E_L already established G_{LT} was the only remaining main driver of circumferential strain and was therefore established via the same method as used for the previous parameters. A full overview of the workflow can be seen as a flowchart in Figure 5.6.

4

Results and discussion

This chapter includes the final results and discussion of the results obtained from simulations and physical testing. Also, the possible sources of errors are discussed and how they could affect the characterized parameters.

4.1 Raw physical test data

Between 15 – 40 kN, all of the axial compression tests have an obvious linear region in both the axial and circumferential strain as seen in Figure 4.1 and Figure 4.2. As mentioned in Section 3.7, when looking at the apparent stiffness and the force/strain slope the results look consistent. The non-linear region in the beginning may occur due to the phenomena of friction causing barreling and/or plastic-like deformation at the edges known as edge crushing. Visual inspection of the specimens after completion did not show any signs of edge crushing, however they were just inspected by eye and not with a microscope since micromechanics was not a point of interest for this study.

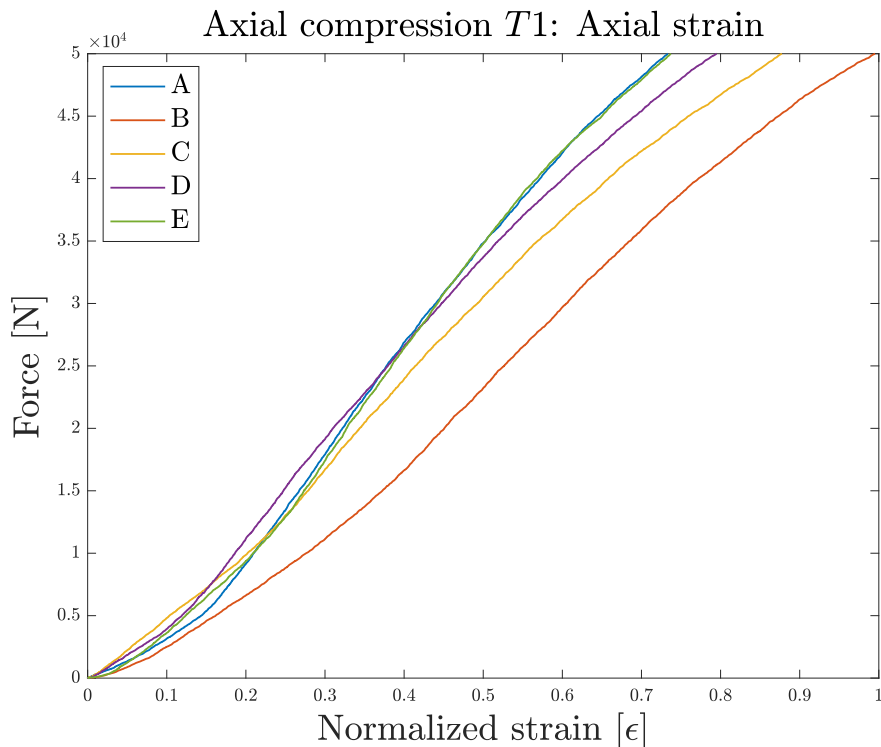


Figure 4.1: Figure showing relation between applied force and measured axial strain for the five test specimens of *T1* in axial compression.

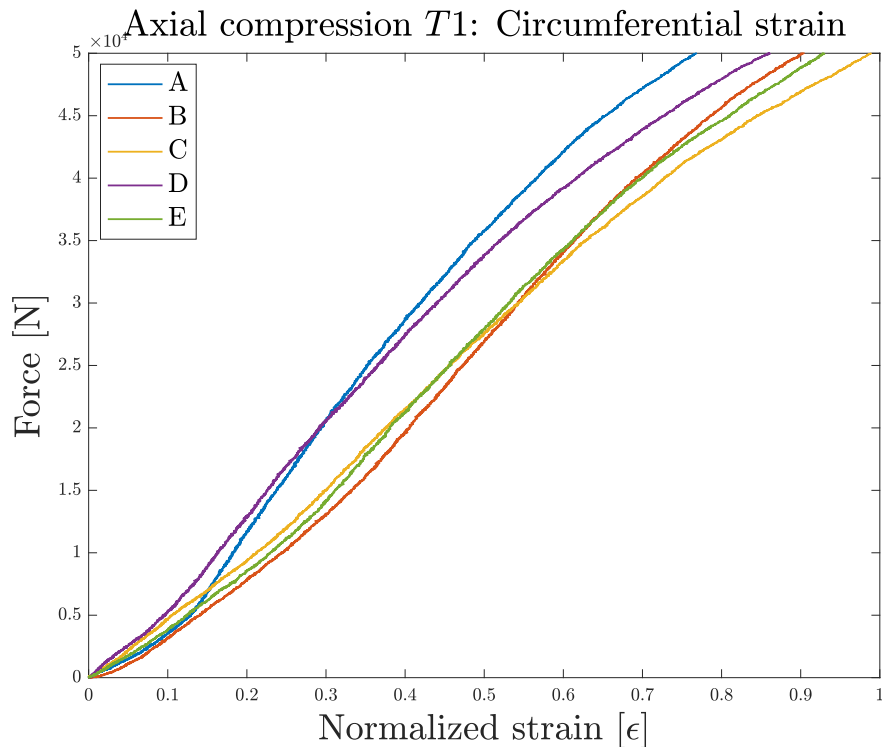


Figure 4.2: Figure showing relation between applied force and measured circumferential strain for the five test specimens of $T1$ in axial compression.

The physical test data from the split hoop have more spread than the axial compression test. As seen in Figure 4.3, four of five curves behave quite linearly after 2.5 kN towards the end. The non-linear behavior in the beginning is most likely due to a combination of elastic deformation of the rings when they conform to the shape of the puck as mentioned in Section 3.6 and friction restricting transverse strain of the specimen. As the specimen are uneven on the inside (due to extra epoxy), it is possible that these surface imperfections might yield additional friction which might create more non-linear behavior as compared to a smooth surface sliding over the pucks.

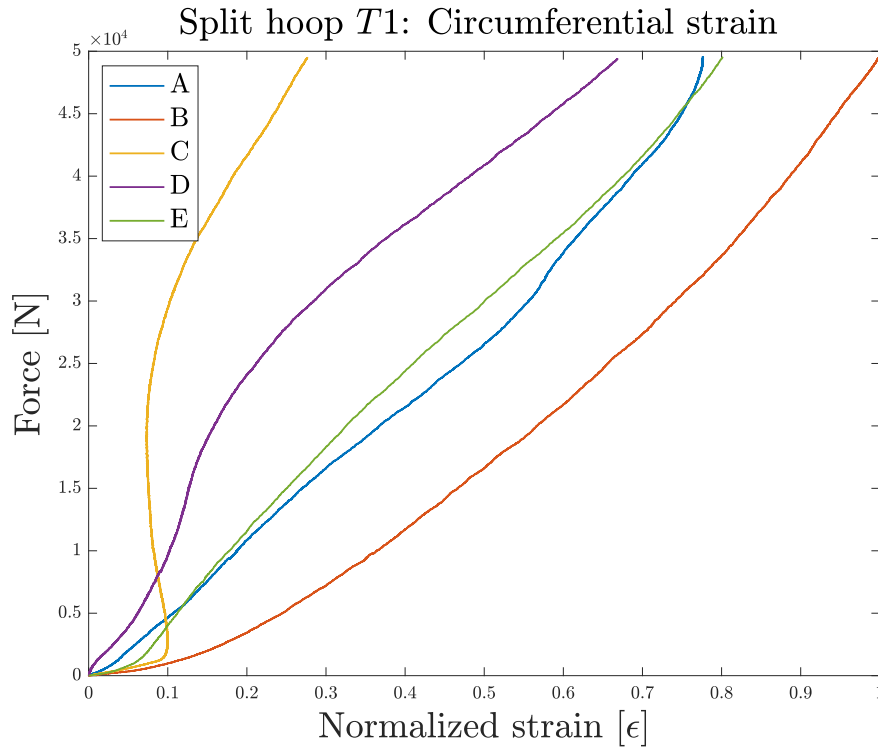


Figure 4.3: Figure showing relation between applied force and measured circumferential strain for the five test specimens of *T1* in the split hoop test.

When looking at the axial strain from the split hoop tests in Figure 4.4, it is clear that the results are very non-linear and kinked. These non-linearities and kinks are believed to have arisen from the effects of friction prohibiting the axial movement of the hoop. Due to this constraint of axial movement a false stiffness presents itself, which makes it hard to analyze and quantify the axial strain results from the split hoop test, especially since the axial strain restriction seems to occur at different load ranges for the different test specimen. When the axial friction passes the limit of static friction, axial strain increases quickly with little added force and hence creating a slope that would propose a lower apparent stiffness. Further non-linearities where the strain decreases with the increase of force presents itself in the curves. This phenomenon is believed to be caused by through-thickness effects or local bending in the axial direction caused by irregularities on the inner surface of the specimen.

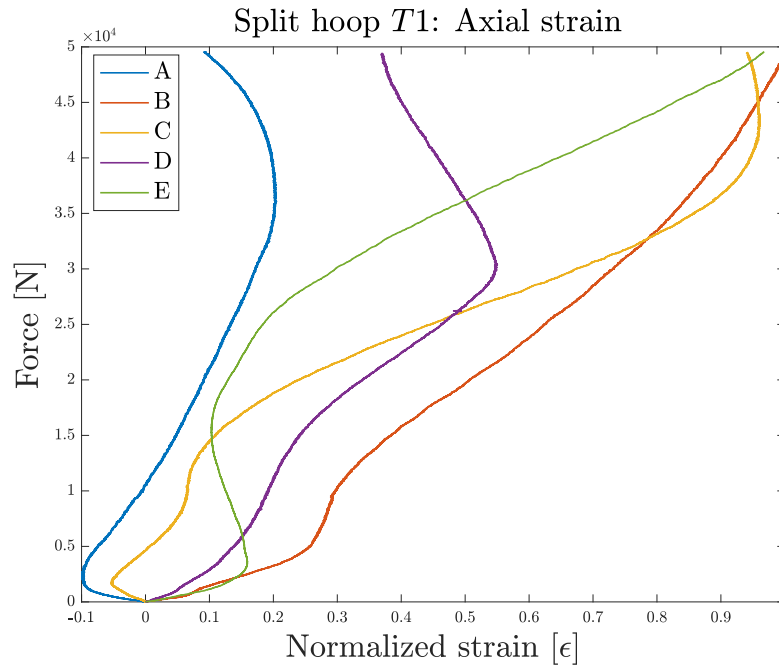


Figure 4.4: Figure showing relation between applied force and measured axial strain for the five test specimens of *T1* in the split hoop test.

As seen in Figure 4.5 the results from the split hoop test for tube *T3* are linear and consistent in the range between 0 – 10 kN. Somewhere in the range between 10 – 15 kN they reach the limit of elastic deformation, some specimens have therefore been tested to 17 kN since a longer test would not result in more information.

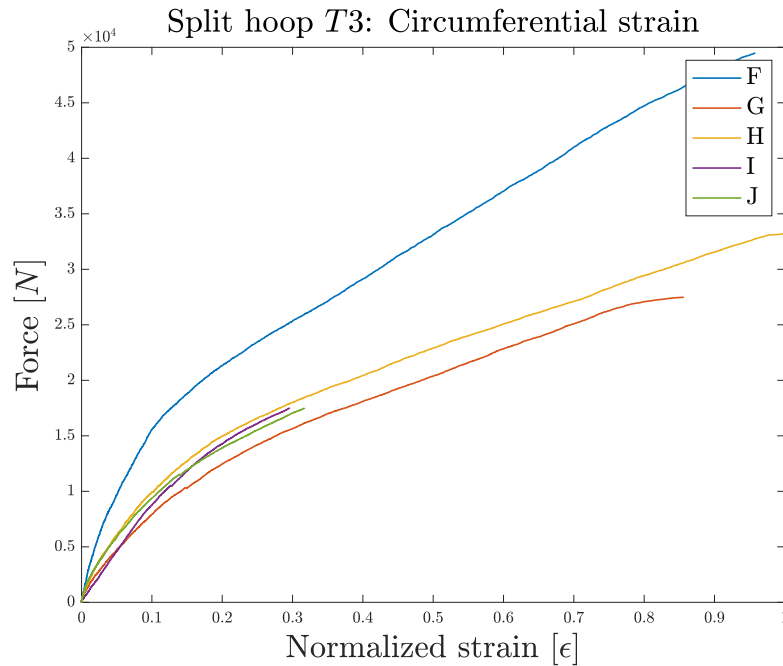


Figure 4.5: Figure showing relation between applied force and measured circumferential strain for the five test specimens of *T3* in the split hoop test.

4.2 Analyzed physical test data

With the method described in Subsection 3.7, the most linear regions of all curves were determined for future analysis. The raw data for the axial compression did not show any unexpected behavior, and according to the R^2 -values the most linear region for both the axial and circumferential strain is between 25 – 35 kN. These regions are represented by the horizontal dotted lines in Figure 4.6 and Figure 4.7. In that interval the mean linear slope is calculated and represented as the black circles plotted as a straight line. This mean linear slope was then used for characterization of material parameters.

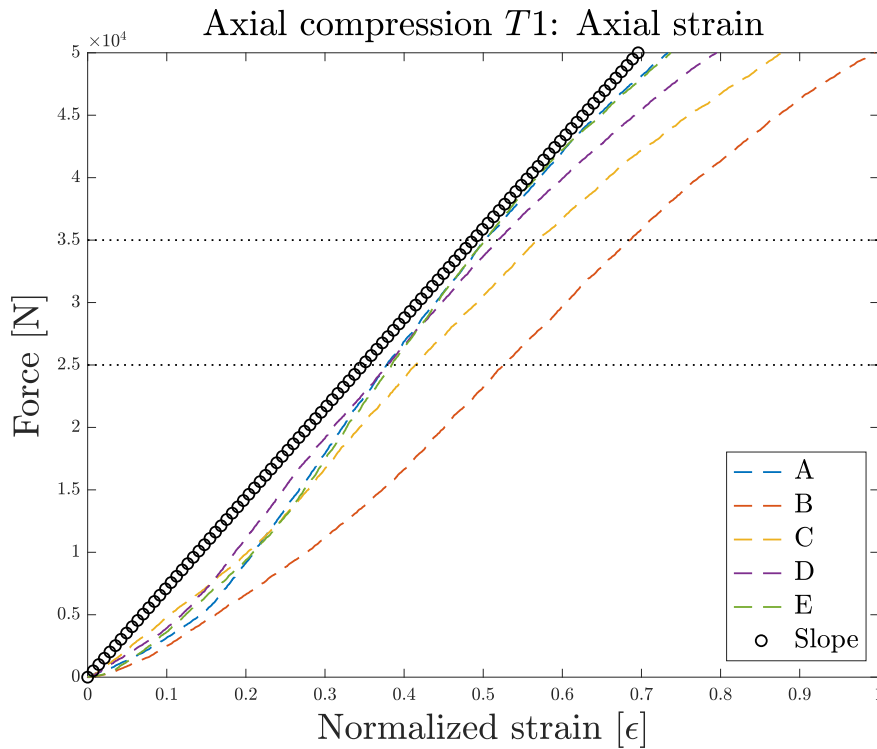


Figure 4.6: Figure showing the most linear force-axial strain relation in the axial compression test on tube $T1$, which occurs in the load region between 25 and 35 kN (indicated by the black dotted lines). The black circles represent an linear response using the mean linear slope in that region.

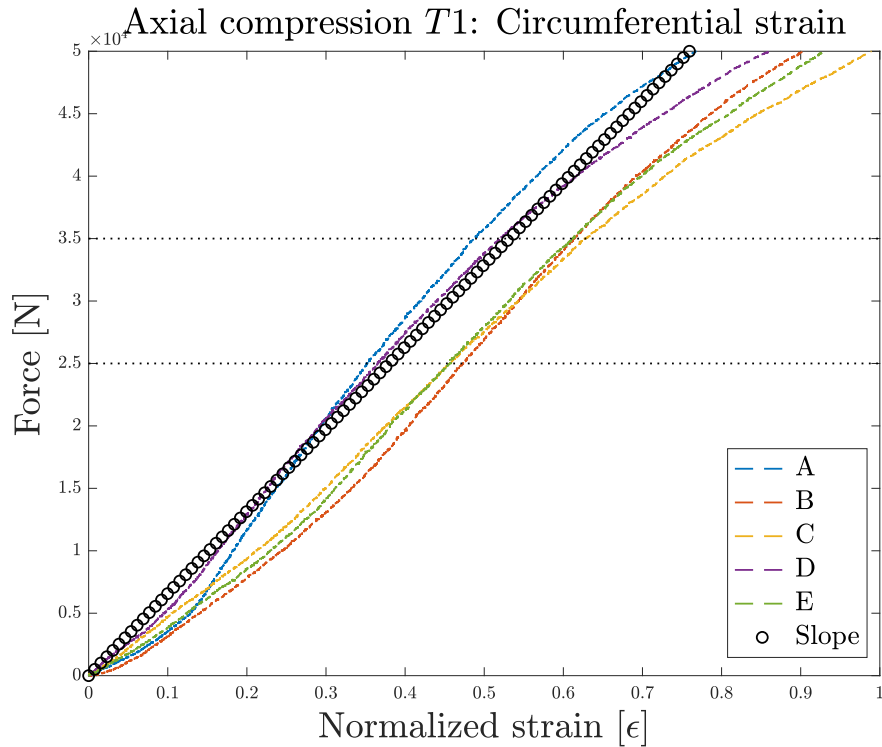


Figure 4.7: Figure showing the most linear force-circumferential strain relation in the axial compression test on tube $T1$, which occurs in the load region between 25 and 35 kN (indicated by the black dotted lines). The black circles represent an linear response using the mean linear slope in that region.

When analyzing the raw data from the split hoop test in Figure 4.3 test specimen C was deemed an outlier. The strange behavior in the beginning of curve C could have something to do with the friction that prevents the ring to slide smoothly at the start. Also, the four other tests have a consistent behavior and slope after 25 kN, judged as acceptable results. As before, the mean slope is then calculated without the data from C even though it is included in Figure 4.8 below.

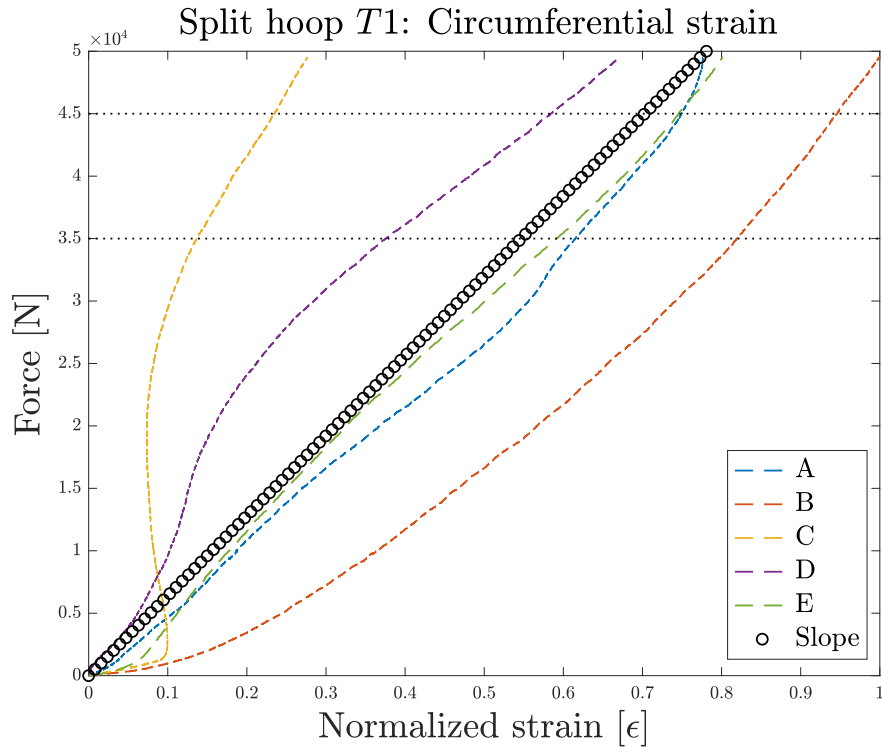


Figure 4.8: Figure showing the most linear force-circumferential strain relation in the split hoop test on tube *T1*, which occurs in the load region between 35 and 45 kN (indicated by the black dotted lines). The black circles represent an linear response using the mean linear slope in that region.

As mentioned in Section 4.1, the axial strain data from the split hoop test on tube *T1* is highly non-linear. Test specimen A was deemed an outlier, probably due to the frictional effects. As for the circumferential data above, curve A is included in Figure 4.9 below even though it is not included in the calculation of the mean linear slope.

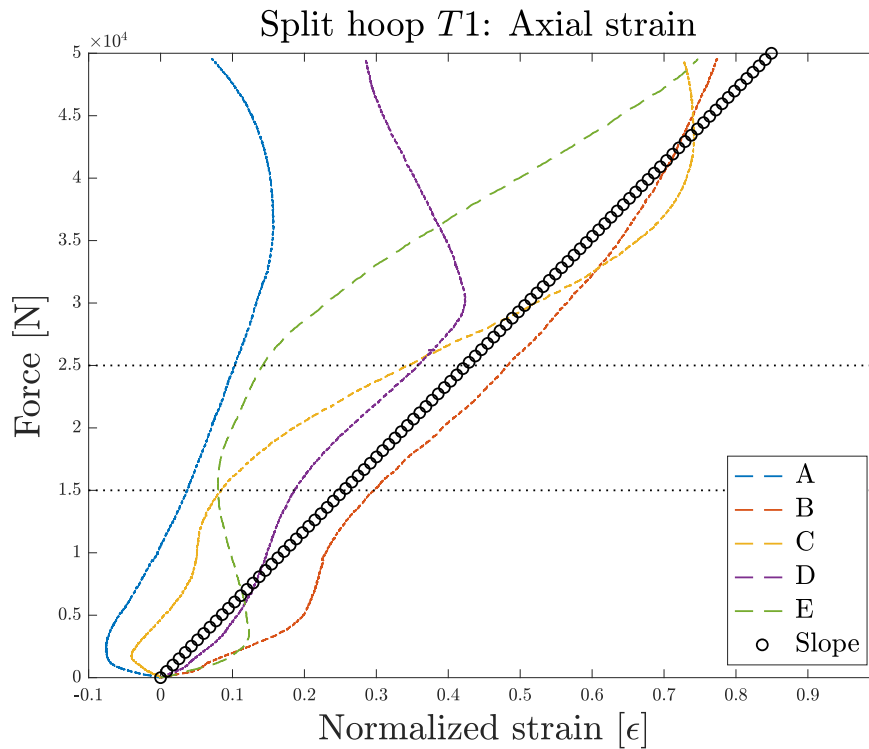


Figure 4.9: Figure showing the most linear force-axial strain relation in the split hoop test on tube $T1$, which occurs in the load region between 15 and 25 kN (indicated by the black dotted lines). The black circles represent an linear response using the mean linear slope in that region.

As for the $T1$ split hoop test, the test of $T3$ to characterize the shear modulus have one significant outlier, as can be seen in Figure 4.10. Four of the results are consistent and therefore curve F will be excluded from the calculations of the mean slope. Furthermore, the specimen reach the yield limit and start to deform permanently after approximately 10 kN which can be seen in Figure 4.5.

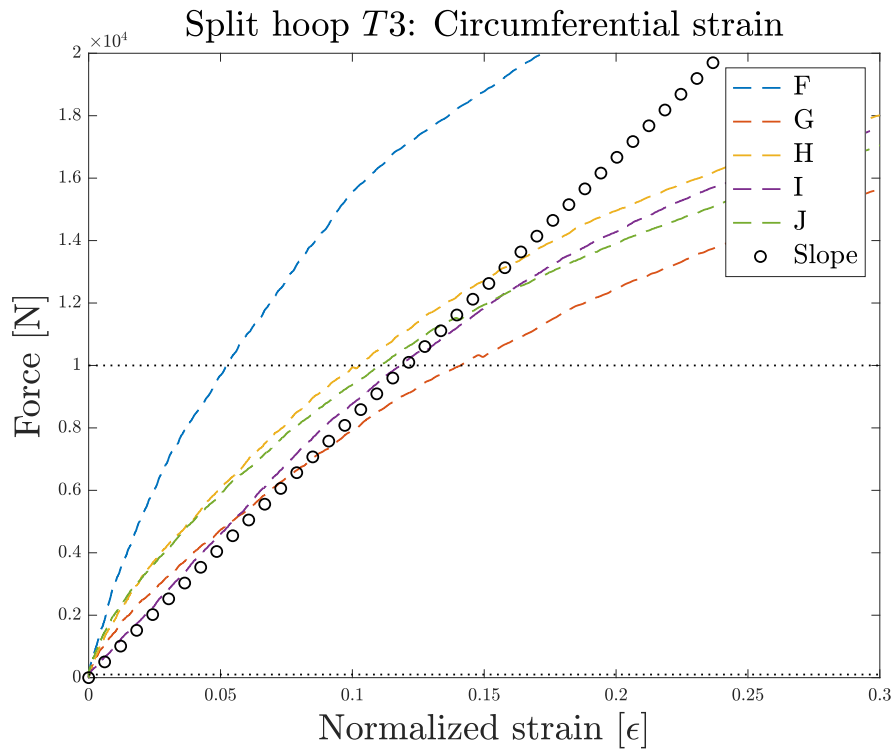


Figure 4.10: Figure showing the most linear force-circumferential strain relation in the split hoop test on tube *T3*, which occurs in the load region between 0 and 10 kN (indicated by the black dotted lines). The black circles represent an linear response using the mean linear slope in that region.

4.3 Final results using characterized parameters

The final results and simulations are presented below in Figure 4.11 - 4.15 where the proposed effects of friction prohibiting strain can be seen in all of the plots. The effects of friction presents itself as non-linear waviness in the curves from where friction prohibits strain, creating a momentary steeper curve and when static friction is overcome; excessive sliding occurs and large strain is seen in the curves, presented as a more gentle slope.

The curves presented as "Final Simulation" in the graphs are the test in question simulated with the final calibrated material properties. The curves denoted as "Slope" are the slopes derived with the method described in Subsection 3.7. The curves A-E are the results from the physical tests.

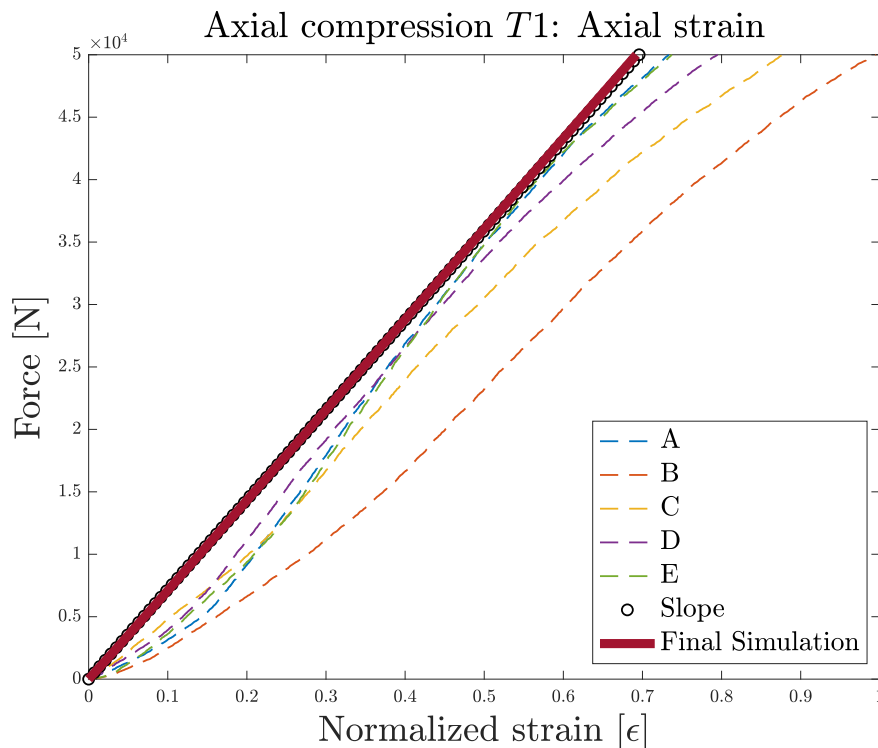


Figure 4.11: Figure showing axial strain on tube $T1$ from both physical test results and a simulation using calibrated material parameters in axial compression.

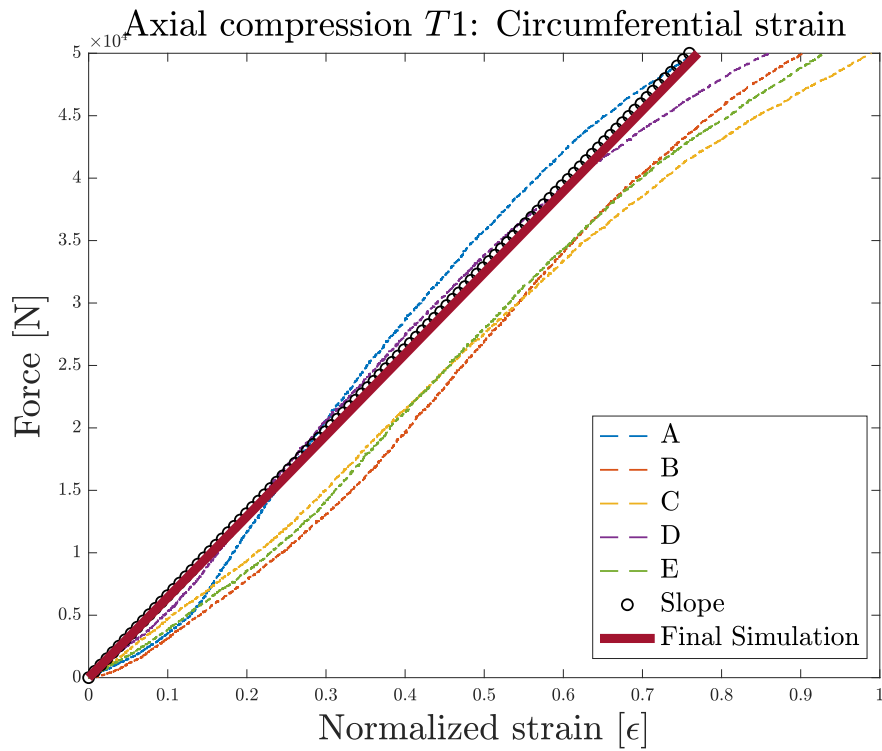


Figure 4.12: Figure showing circumferential strain on tube $T1$ from both physical test results and a simulation using calibrated material parameters in axial compression.

The effect of difference in pre-tension area of the model and test results can be seen clearly in the split hoop test (Figure 4.13), where the curve of the final simulation is shifted to the right approximately 10 – 20% while the slope matches well for the remaining data.

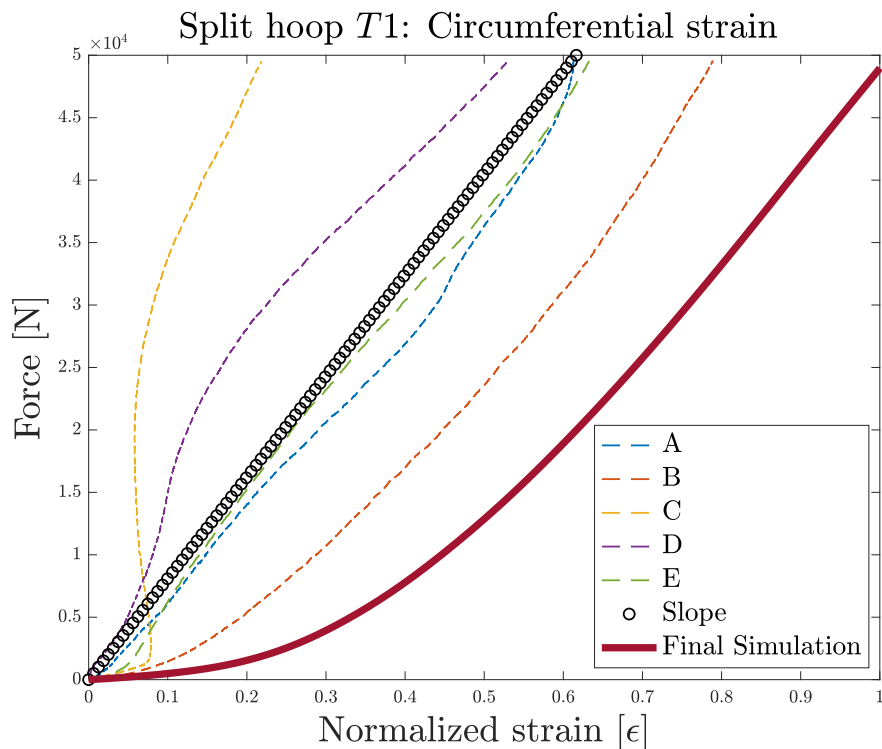


Figure 4.13: Figure showing circumferential strain on tube $T1$ from both physical test results and a simulation using calibrated material parameters in the split hoop test.

As seen in Figure 4.14 and discussed in Subsection 3.8 the axial strain data from the split hoop tests are highly non-linear and it was hence decided to characterize ν_{LT} using both axial compression and split hoop tests. The Poisson ratio from split hoop simulations are in the low ranges of general fiber reinforced polymer Poisson's ratios while ν_{LT} extracted from the compression simulation is in the high range of composite Poisson's ratios. The final simulation is done with the Poisson ratio determined in the compression test, and it can be seen in Figure 4.14 that the axial force-strain response from the split hoop simulation does not match the suggested average slope from the physical tests. If ν_{LT} characterized from the split hoop test was to be used a similar discrepancy as the one seen in Figure 4.14 would instead be seen in the circumferential response of the compression test seen in Figure 4.12.

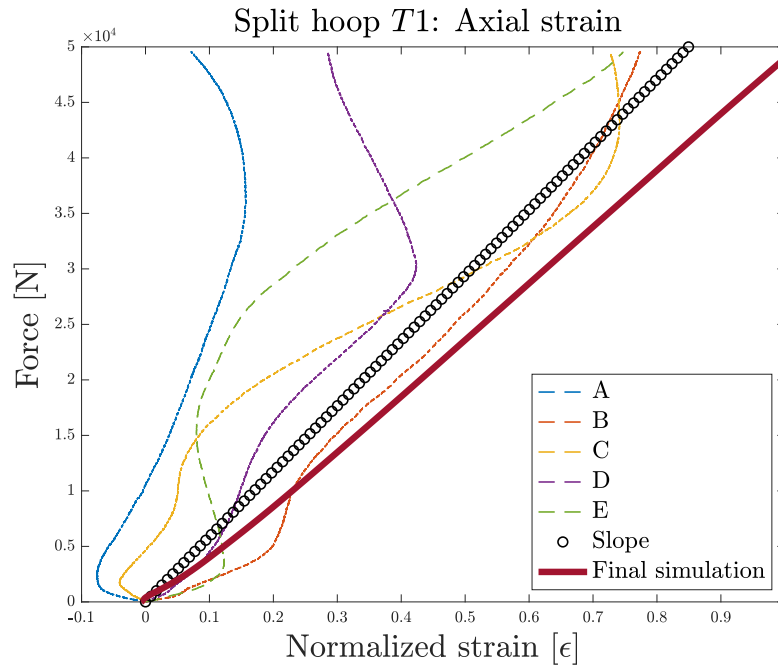


Figure 4.14: Figure showing axial strain on tube $T1$ from both physical test results and a simulation using calibrated material parameters in the split hoop test.

As seen in Figure 4.15, the circumferential strain depended on the characterized shear modulus coincide well with the physical test results in the linear region. The initial non-linear region from 0 – 3 kN is likely due to friction.

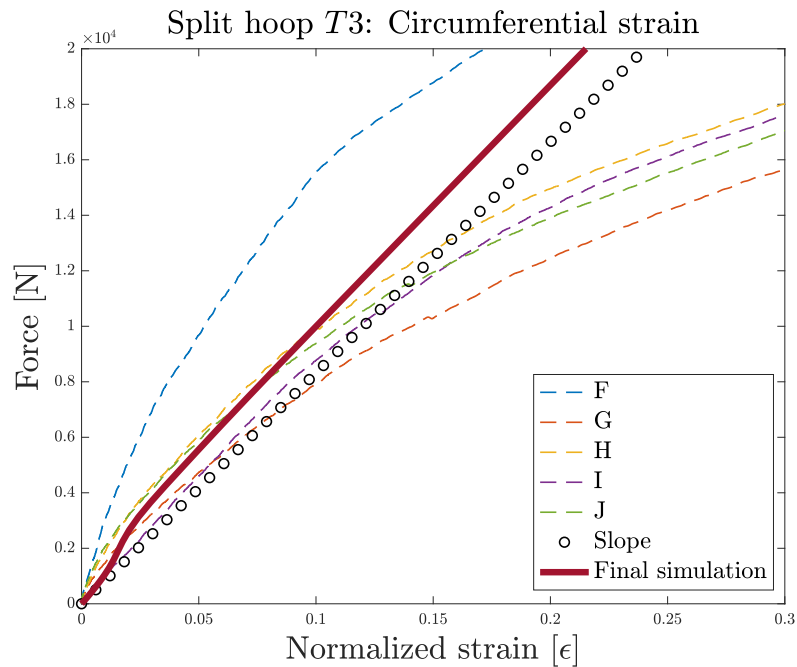


Figure 4.15: Figure showing circumferential strain on tube $T3$ from both physical test results and a simulation using calibrated material parameters in the split hoop test.

4.4 Sources of error

The main error source detected for this method is friction. In all test results some non-linearities and humps were observed and thus it is believed that the frictional effects could have had a significant influence on the measured force-strain relations, and thereby also on the characterized parameters. This phenomena would have an effect on the different moduli and also affect ν_{LT} since it's characterization is also heavily affected by E_T or E_L depending on what test is used for characterization of ν_{LT} . As mentioned in Subsection 4.3 the final value of ν_{LT} is highly dependent on what test is used and hence should be investigated more thoroughly before proceeding. However it is believed that the split hoop test is the most suitable for characterizing ν_{LT} as discussed in Subsection 3.2.4 and that more reliable results would be achieved if the issue of friction could be resolved.

Another source of error is believed to be the uneven shape of the inner specimen surface, as discussed in Section 3.1 and 4.1. These humps on the surface may be acting as fulcrums, creating bending moments as they raise the specimen from the surface of the puck. The humps are also believed to add to the frictional effects where they could deform and create ridges for the steel pucks to dig into.

A major source of error is of course the FE-model itself since it by no means is a perfect representation of reality. Since the surface finish of the pucks were machined, further investigation into communicating this into the model might add accuracy to the model.

Additionally the manner in which the force/strain slope is extracted from the physical test data could be refined since frictional effects are seen within the 10 kN range used in Subsection 3.7, a mean slope of a larger load range could for example smooth out some of the non-linear curvatures which the current way of extracting data might have picked up. Since it is believed that axial strain in the split hoop test results is held up by friction and then in a spring-like effect exaggerated when additional force is added, a mean slope over a larger range might cancel out these two effects

Furthermore, an interesting although time consuming idea would be to extract material values for each individual specimen and analyze the results from those in order to better analyze the spread of the samples and testing. A final source of error which is hard to assess is the ply angle of each lamina which it might have been skewed in the manufacturing process. This angular discrepancy is quite hard to measure after the fact since the layers are embedded in the specimen [37], [38].

Like the misalignment of fiber angles; the misalignment of strain gauges is a possible source of error. However, the misalignment of the strain gauges is possible to measure geometrically and taken into consideration if the results are linear. The strain data presented in this thesis however was considered to non-linear to investigate in this manner.

5

Conclusion and proposed validation

5.1 Investigation of potential validation

Validation of the method at hand is required before using this method in a commercial setting. With help from the validation and more suitable testing apparatus the main error sources of this project; friction and boundary condition effects can be further investigated and controlled for future testing. Furthermore a wider variety of material systems together with larger sample sizes for physical testing would further improve this method for future use. Since it was possible to isolate each material property a less complex optimization algorithm than *fminsearch* could probably be used to decrease computational time.

Due to the delays and financial issues discussed in Section 1 no validation experiments were performed for this project. However, a bi-axial tension-torsion test was investigated for feasibility as a validation test. The test in question a *T2* tube was simulated for simultaneous axial tension up to 50 kN and torsion of 1 kNm. The resulting force-torque-strain relations are shown in Figures 5.1-5.5 along with their variation due to changes in the material parameters. The resulting shear strain is believed to be mainly affected by G_{LT} , and its sensitivity is shown in Figure 5.5. Furthermore axial and circumferential strains are both believed to be influenced by E_L (see sensitivity study in Figures 5.1-5.2) while the circumferential strain is believed to be affected also by ν_{LT} and E_T (see Figures 5.3-5.4). In all respective cases, a strong sensitivity to the main parameters is observed, which indicates that the proposed test could be a good test for validating the characterised properties. One should however consider to use a long enough specimen so that the effects of the boundary conditions can be neglected. Furthermore as the effects of friction are not present for this type of bi-axial test, this major source of uncertainty could be excluded for this test.

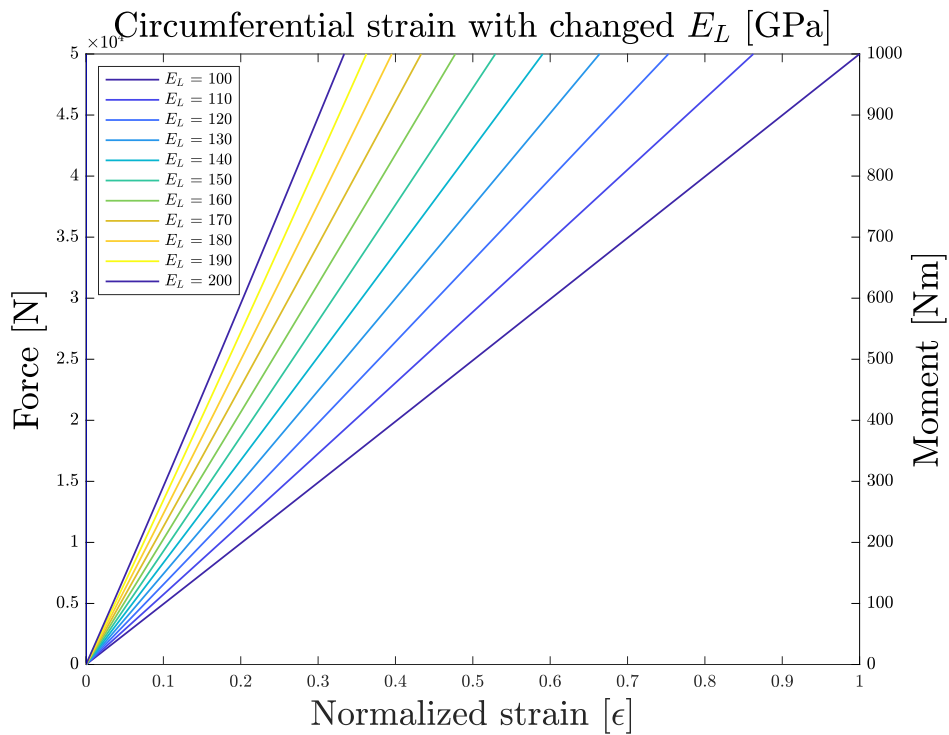


Figure 5.1: Numerical response of the proposed bi-axial validation test showing the evolution of circumferential strain as a function of increasing load, and its sensitivity to the longitudinal stiffness E_L .

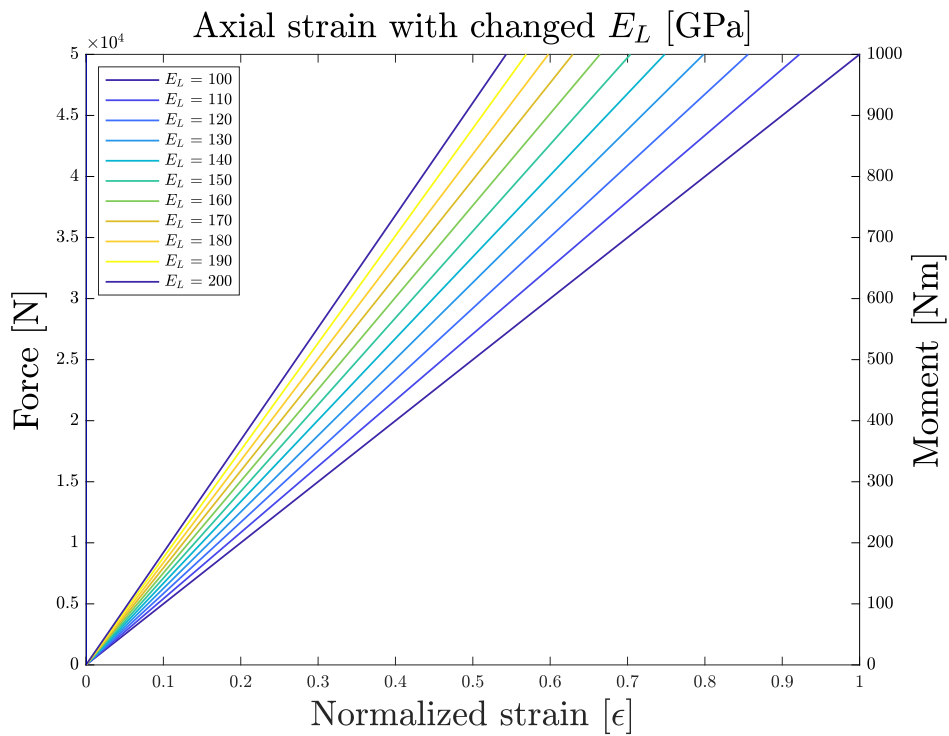


Figure 5.2: Numerical response of the proposed bi-axial validation test showing the evolution of axial strain as a function of increasing load, and its sensitivity to the longitudinal stiffness E_L .

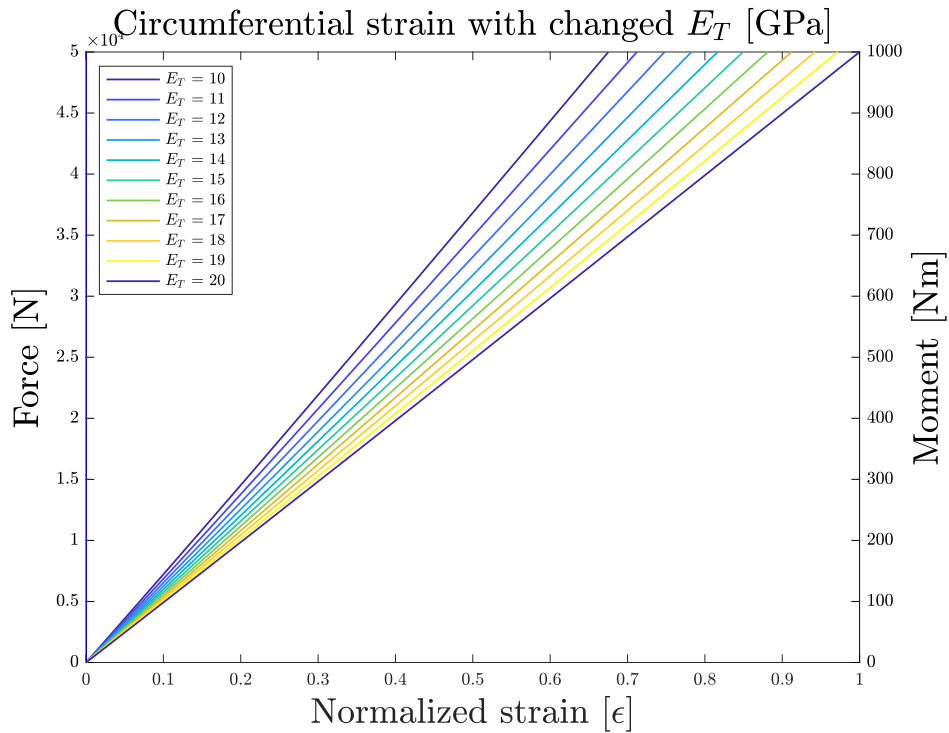


Figure 5.3: Numerical response of the proposed bi-axial validation test showing the evolution of circumferential strain as a function of increasing load, and its sensitivity to the transverse stiffness E_T .

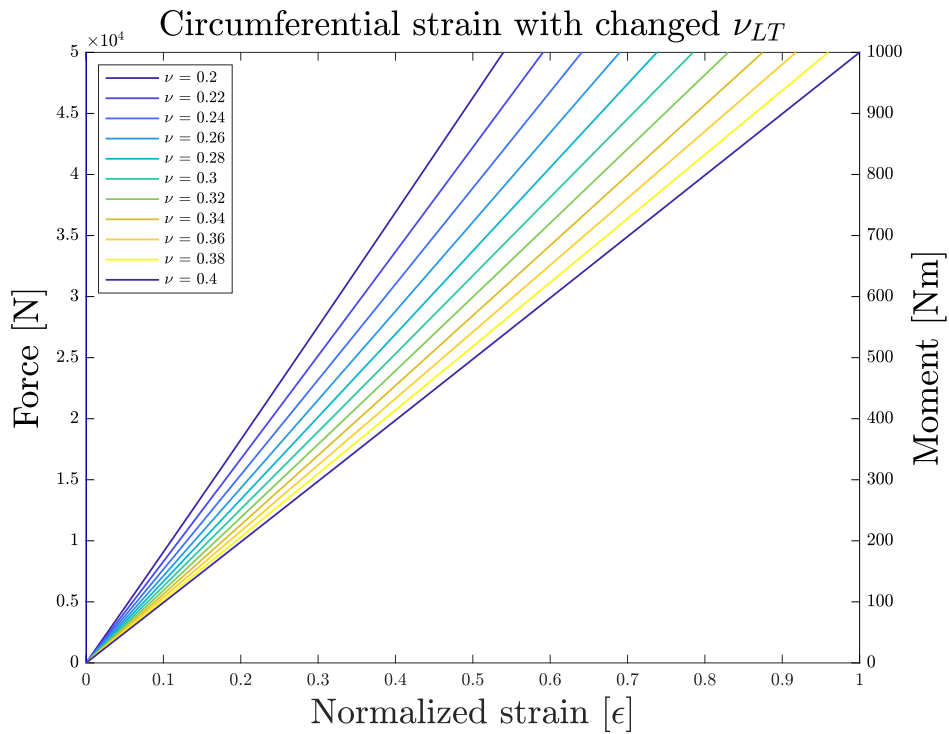


Figure 5.4: Numerical response of the proposed bi-axial validation test showing the evolution of circumferential strain as a function of increasing load, and its sensitivity to the Poisson's ratio ν_{LT} .

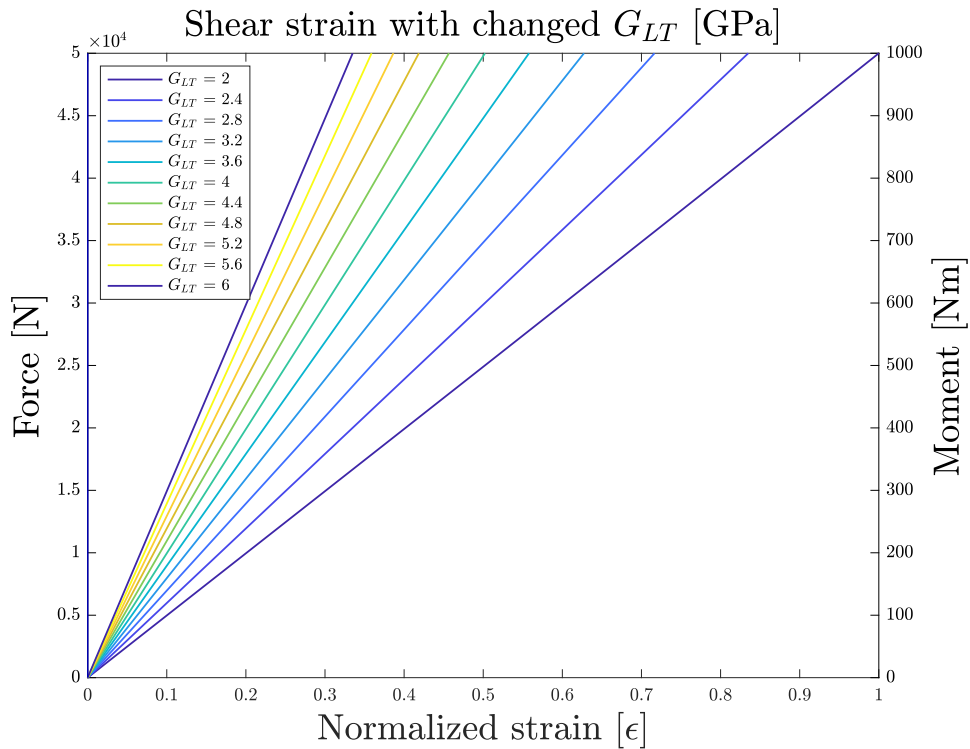


Figure 5.5: Numerical response of the proposed bi-axial validation test showing the evolution of shear strain as a function of increasing load, and its sensitivity to the shear modulus G_{LT} .

5.2 Conclusion

While the method developed in this thesis is no where near perfect it is believed to be a good starting point both for further method refinement as well as for decent characterization of the elastic in-plane properties. However, further investigation and validation is needed before finalizing the method. The final workflow of this method can be seen below in Figure 5.6. The Poisson's ratio showed to be the hardest parameter to extract, and as discussed in Section 4.3 ν_{LT} had a wide spread depending on what experiment was used to extract it. This suggest that it might be the same effects of friction that presents itself in both tests since it looks to be skewing the split hoop test in one direction and the compression test in another. This suggests that the real Poisson's ratio is somewhere in between the two extremes.

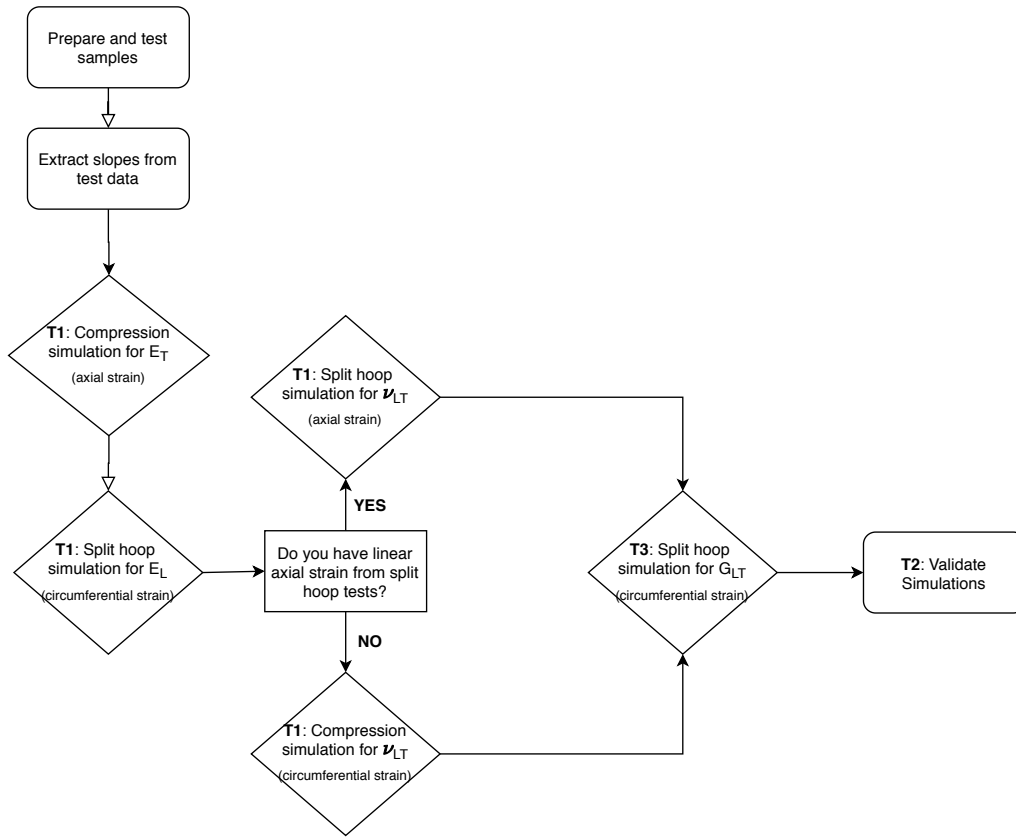


Figure 5.6: Flowchart of the proposed workflow of the method created in this thesis

5.3 Future considerations

Friction is regarded as the main driver of error in this method and hence measures for reducing friction should definitely be prioritized when using or refining this method for material characterization. It is theorized that polishing the machined surface of the pucks, mainly in the split hoop test will make a large difference on the non-linear behavior of the axial strain response. Additionally being able to reverse the test machine in the same manner that force is applied would give a good view of the frictional effects and how to counteract them. If it is seen from further analysis that the frictional effects are hard to avoid in the physical tests, a soft contact model between the steel pucks and the epoxy surface of the ring could be a good way to further add to the accuracy of the simulation model.

As mentioned in Section 5.1 there is a need for validation, however since there are obvious and known sources of error these should be addressed, prior to locating time and resources towards validation. After the issue of friction is addressed the large difference in ν_{LT} between compression and split hoop extraction (seen in Figure 4.14) should be investigated further.

Bibliography

- [1] SIMULIA Abaqus, *Abaqus integration points*, 2020. [Online]. Available: <https://abaqus-docs.mit.edu/2017/English/SIMACAERefImages/adv-layups-sectionpoints-nls.png>
- [2] *Eight-node brick element (C3D8 and F3D8)*, 2020. [Online]. Available: http://web.mit.edu/calculix_v2.7/CalculiX/ccx_2.7/doc/ccx/node26.html
- [3] *Eight-node brick element with reduced integration (C3D8R and F3D8R)*, 2020. [Online]. Available: http://web.mit.edu/calculix_v2.7/CalculiX/ccx_2.7/doc/ccx/node27.html
- [4] *Twenty-node brick element (C3D20 and F3D20)*, 2020. [Online]. Available: http://web.mit.edu/calculix_v2.7/CalculiX/ccx_2.7/doc/ccx/node29.html
- [5] Majid Tanbakuei Kashani, *Second-order solid element reduced integration C3D20R*, 2020. [Online]. Available: https://www.researchgate.net/profile/Majid_Tanbakuei_Kashani/publication/319350606/figure/fig10/AS:532928015683585@1504071348351/10-Second-order-quadratic-solid-elements-A-reduced-integration-C3D20R-8-integration.png
- [6] B. Alcock, N. Cabrera, N.-M. Barkoula, J. Loos, and T. Peijs, “The mechanical properties of unidirectional all-polypropylene composites,” *Composites Part A: Applied Science and Manufacturing*, vol. 37, pp. 716–726, 2006.
- [7] G. Perillo, R. Vacher, F. Grytten, S. Sørbo, and V. Delhaye, “Material characterisation and failure envelope evaluation of filament wound gfrp and cfrp composite tubes,” *Polymer Testing*, vol. 40, pp. 54 – 62, 2014.
- [8] R. Gopal, R. Gettu, and B. Bharatkumar, “Modified split disk test for characterization of frp composites,” *Journal of Structural Engineering (Madras)*, vol. 477, pp. 477–487, 2016.
- [9] R. Carter, “Characterizing the mechanical properties of composite materials using tubular samples,” Ph.D. dissertation, Virginia Polytechnic Institute and State University, 2001.
- [10] A. Kastenmeier, V. Schmid, and I. Ehrlich, “Specimen preparation and material characterization of filament wound composite tubes,” *ATINER’s Conference Paper Series*, vol. IND2016-1077, 2016.
- [11] F. D. L. G. M. Crozatier, S. Terekhina, “Mechanical characterization of composite materials from curved structures,” *Archive ouverte HAL*, 2016.

- [12] M. Fagerström, “Lecture notes: Composite mechanics, Chalmers University of Technology,” 2019.
- [13] “Abaqus analysis user’s guide: 28.1.1 solid (continuum) elements,” 2020. [Online]. Available: <http://dsk.ippt.pan.pl/docs/abaqus/v6.13/books/usb/default.htm?startat=pt06ch28s01alm01.html>
- [14] *Twenty-node brick element with reduced integration (C3D20R and F3D20R)*, 2020. [Online]. Available: http://web.mit.edu/calculix_v2.7/CalculiX/ccx_2.7/doc/ccx/node30.html
- [15] *ASTM D-2290*, 2020. [Online]. Available: <http://www.astm.org/cgi-bin/resolver.cgi?D2290>
- [16] *ASTM D-2412*, 2020. [Online]. Available: [http://www.astm.org/cgi-bin/resolver.cgi?D2412-11\(2018\)](http://www.astm.org/cgi-bin/resolver.cgi?D2412-11(2018))
- [17] Dassault Systèmes Simulia Corp, “Abaqus CAE 6.14,” 2020. [Online]. Available: <https://www.3ds.com/products-services/simulia/products/abaqus/abaquscae/>
- [18] B. D. Agarwal, L. J. Broutman, and K. Chanshekhara, *Analysis and performance of fiber composites*, 2018.
- [19] J. Anderson and M. Altan, “Bladder Assisted Composite Manufacturing (BACM): Challenges and Opportunities,” 2014.
- [20] VPG, Vishay, *C2A-06-031WW-350*, 2020. [Online]. Available: <http://www.vishaypg.com/docs/11250/031ww.pdf>
- [21] A. Schranzinger, “Modeling of long-fiber-reinforced composites in Abaqus,” Master’s thesis, Graz University of Technology, 2014.
- [22] E. Barbero, *Finite Element Analysis of Composite Materials*. CRC Press, 2008.
- [23] Dassault Systèmes Simulia Corp, *Abaqus Docs*, 2020. [Online]. Available: ivt-abaqusdoc.ivt.ntnu.no:2080/v6.14/books/usi/pt03ch12s13h1b04.html
- [24] I. Krucinska and T. Stypka, “Direct measurement of the axial poisson’s ratio of single carbon fibres,” *Composites Science and Technology*, vol. 41, no. 1, pp. 1 – 12, 1991.
- [25] H. Cease, P. Derwent, H. Diehl, J. Fast, and D. Finley, “Measurement of mechanical properties of three epoxy adhesives at cryogenic temperatures for ccd construction,” *FERMILAB-TM-2366-A*, 2006.
- [26] *Friction and Friction Coefficients*, 2020. [Online]. Available: https://www.engineeringtoolbox.com/friction-coefficients-d_778.html

-
- [27] H. Dhieb, J. Buijnsters, F. Eddoumy, and J.-P. Celis, “Surface damage of unidirectional carbon fiber reinforced epoxy composites under reciprocating sliding in ambient air,” *Composites Science and Technology*, vol. 71, pp. 1769–1776, 2011.
- [28] J. Leon Becerra, A. Pertuz, and O. González Estrada, “Stress analysis , first ply failure and damage of a multilayer composite pipe for different boundary conditions,” in *ESSS Convergence Colombia 2017*. GIEMA, School of Mechanical Engineering, Universidad Industrial de Santander, Colombia, 2017.
- [29] VPG, Vishay, *M-Bond AE-10*, 2020. [Online]. Available: <http://www.vishaypg.com/docs/11011/bondae10.pdf>
- [30] VPG, Vishay, *M-Bond 200*, 2020. [Online]. Available: <https://docs.micro-measurements.com/?id=6671>
- [31] Bent Tram, *Bent Tram UCT50*, 2020. [Online]. Available: <https://benttram.com/uct-universal-compression-and-tension-testing-machine/>
- [32] S.-H. Yoon, C.-G. Kim, and W.-M. Cho, “Measurement of tensile properties using filament wound ring specimens,” *Journal of Reinforced Plastics and Composites*, vol. 16, no. 9, pp. 810–824, 1997.
- [33] LORD Sensing, “Lord v-link 200,” 2020. [Online]. Available: <https://www.microstrain.com/wireless/V-LINK-200>
- [34] Mathworks, MATLAB, *fminsearch*, 2020. [Online]. Available: <https://www.mathworks.com/help/optim/ug/fminsearch.html>
- [35] Mathworks, MATLAB, *fmincon*, 2020. [Online]. Available: <https://www.mathworks.com/help/optim/ug/fminsearch.html>
- [36] Python, *Python 3.8*, 2020. [Online]. Available: <https://www.python.org/>
- [37] L. Nelson, R. Smith, and M. Mienczakowski, “Ply-orientation measurements in composites using structure-tensor analysis of volumetric ultrasonic data,” *Composites Part A: Applied Science and Manufacturing*, vol. 104, pp. 108 – 119, 2018.
- [38] M. Wisnom, “The effect of fibre misalignment on the compressive strength of unidirectional carbon fibre/epoxy,” *Composites*, vol. 21, no. 5, pp. 403 – 407, 1990.

